



Numerical investigation of the mechanism of granular flow impact on rigid control structures

Edward Yang^{1,2} · Ha H. Bui^{1,2} · Giang D. Nguyen³ · Clarence E. Choi⁴ · Charles W. W. Ng⁵ · Hans De Sterck⁶ · Abdelmalek Bouazza²

Received: 8 June 2020 / Accepted: 4 February 2021 / Published online: 24 February 2021
© The Author(s), under exclusive licence to Springer-Verlag GmbH, DE part of Springer Nature 2021

Abstract

Baffles and check-dam systems are often used as granular flow (rock avalanches, debris flows, etc.) control structures in regions prone to dangerous geological hazards leading to massive landslides. This paper explores the use of numerical modelling to simulate large volume granular flow and the effect of the presence of baffles and check dam systems on granular flow. In particular, the paper offers a solution based on the smoothed particle hydrodynamics numerical method, combined with a modified Bingham model with Mohr–Coulomb yield stress for granular flows. This method is parallelised at a large scale to perform high-resolution simulations of sand flowing down an inclined flume, obstructed by rigid control structures. We found that to maximise the flow deceleration ability of baffle arrays, the design of baffle height ought to reach a minimum critical value, which can be quantified from the flow depth without baffles (e.g. 2.7 times for frictional flows with friction angle of 27.5°). Also, the check-dam system was found to minimise run-out distances more effectively but experiences substantially higher forces compared to baffles. Finally, flow-control structures that resulted in lower run-out distances were associated with lower total energy dissipation, but faster kinetic energy dissipation in the granular flows; as well as lower downstream peak flow rates.

Keywords Baffles system · Check-dam system · Control structures · Debris flows · Granular flows · SPH

1 Introduction

Channelised debris flows can occur due to volcanic activity (lahar) [1], and more commonly due to heavy rainfall [2]. They lead to significant direct and indirect costs such as loss of life, destruction of infrastructure, and reduced economic activity [2, 3]. Debris flows are problematic due to the high speeds and greater impact forces that result from channelisation [4]. However, because of their tendency to follow channel-like topography such as rivers or mountain crevices, community decision-makers and planners can protect their communities or points of interest by installing protective measures. For example, check dams are a typical protective measure built to impede oncoming debris flows [5]; or flexible barriers, which aims to stop larger debris [6, 7]. In channelised flows, it is not unusual to install multiple protective measures in series within the same channel to create a cascading effect to dissipate flow kinetic energy and progressively arrest a large torrent (such as in [8, 9]). Furthermore, other structures may be used to

✉ Ha H. Bui
Ha.Bui@monash.edu

¹ Monash Computational Geomechanics (MCG) Lab, Monash University, Melbourne, Australia

² Department of Civil Engineering, Monash University, Melbourne, Australia

³ School of Civil, Environmental and Mining Engineering, University of Adelaide, Adelaide, Australia

⁴ Department of Civil Engineering, The University of Hong Kong, Hong Kong, SAR, China

⁵ Department of Civil and Environmental Engineering, The Hong Kong University of Science and Technology, Hong Kong, SAR, China

⁶ Department of Applied Mathematics, University of Waterloo, Waterloo, Canada

dissipate the energy of the flows before impact with a rigid barrier. In Europe, ‘braking mounds’ can be used to slow down avalanches and debris flows [10, 11], or in [8] where ‘debris flow breakers’ are installed in a stilling basin prior in front of a levee. Another example is in Hong Kong [12] where ‘baffles’ are used for a similar purpose, or to decelerate flows before impacting a rigid barrier (Fig. 1). However, studies on baffles (especially under channelised conditions) are limited in the literature, and the guidelines that mention baffles are largely empirical and prescriptive (e.g. [13, 14]).

Studying debris flows at the field scale, in general, is difficult due to the cost and effort associated with constructing such large-scale facilities (a notable attempt is in [15]). Usually, scaled-down laboratory experiments are used instead. These can be experiments that reflect the topography of a particular region of interest (such as in [16]), or inclined flume experiments that would be aimed at studying debris flows. However, flow information cannot be as easily measured compared to numerical studies, collecting sufficiently detailed data is challenging, significant labour is required to ensure the accuracy of the collected data, and scaling laws may not be well established. Numerical methods offer a complementary approach and are usually more flexible and easier for setting up multiple geometric cases. Grid-based methods such as the finite element method (FEM) or finite volume method (FVM) are well-established methods commonly used in engineering. Still, they can encounter challenges related to grid distortion when simulating large deformation problems. Particle-based continuum methods were introduced to overcome these issues. These methods include the particle finite element method (PFEM) [17, 18] or material point method (MPM) [19], which use material points to carry material information and for which equations are solved on a background mesh in a way not unlike FEM. The advantage of these methods is that the use of particles makes them

inherently adaptive to the deformation of the continuum, while also inheriting properties of the well-established mesh-based methods. Another class of numerical method is the meshless method, such as the smoothed particle hydrodynamics (SPH) method [20, 21] and the discrete element method (DEM) [22]. DEM treats each element as discrete particles, and thus is known as a discontinuum method. The particles interact by collisions, making the method useful in modelling granular systems, but not leaving much in common with most other numerical methods. SPH is a purely meshless method, similar to other particle-based continuum methods in that information is carried by material points. SPH does not use any underlying grid to solve governing equations, but instead uses statistical interpolation techniques. SPH is a relatively mature method with the first papers being published in 1977 by [20, 21] with the main application being to astrophysics. Applications broadened in the 80 s and 90 s including physics of solids and fluids (e.g. [23, 24]), before the method being applied to granular materials [25], debris flows [26], slope failures [27, 28], coupled soil–water interactions [29, 30], and fracturing of geomaterials [31–33]. The applicability of SPH to granular flows has also been demonstrated widely in the literature [34–43], which all shows good agreement with experimental results when the numerical method is coupled with elasto-plastic or visco-plastic constitutive laws. Furthermore, the method has also been shown to be capable of simulating soil–structure interaction problems as in [37, 39, 44, 45]. Given SPH has an established suitability in modelling problems that are similar to obstruction of channelised debris flow, we adopt the method in this work.

In cases where significant scale differences exist between baffle sizes and flow volumes, a sufficiently accurate simulation requires high resolution, which would not be practical for a serial SPH program, high-resolution being necessary to capture the complexities of momentum



Fig. 1 Baffles used in Hong Kong to delay debris flows in conjunction with a flexible barrier system (left) and a rigid barrier (right)

exchange due to earth pressure, drag, and dead zones (i.e. static deposits) behind each baffle [46]. However, in recent years, parallel codes have been developed so that high-resolution simulations capable of millions of SPH particles are now possible [47–50]. This paper explores the use of the granular flow code described in [48], where the parallelisation of elasto-plastic and visco-plastic codes is presented, to study the mechanism of baffles delay of granular flows. The code is first calibrated and validated against laboratory-scale flume experiments with sand conducted in [4, 51] to ensure it can capture essential physics of fast granular flows impacting against baffles. We then take advantage of the flexibility and the ability to obtain detailed information about the flows, to further investigate the influence of increased baffle height on delaying the granular flows, and the mechanism by which baffles impede the flows. Where similar investigations and simulations have been performed by other continuum methods [52, 53], besides not having been done at high-resolution, they have also yet to focus on the use of baffles under channelised conditions, where the dynamics become more complicated due to the momentum exchange resulting from drag, earth pressure and dead zones, and granular vacuums, which do not need to be considered in un-channelised conditions. This therefore necessitates the high-resolution simulations requiring a parallelised SPH code.

2 Numerical scheme

2.1 Governing equations and SPH discretisation

To model granular materials in a continuum SPH framework, the following governing equations consisting of the mass and momentum conservation equations are used, respectively:

$$\frac{D\rho}{Dt} = -\frac{1}{\rho} \nabla \cdot \mathbf{v}, \quad (1)$$

$$\frac{D\mathbf{v}}{Dt} = \frac{1}{\rho} \nabla \cdot \boldsymbol{\sigma} + \mathbf{g}, \quad (2)$$

where $\frac{D(\cdot)}{Dt}$ is the material time derivative of (\cdot) ; ρ is the bulk material density; \mathbf{v} is the velocity vector; $\boldsymbol{\sigma}$ is the Cauchy stress tensor; and \mathbf{g} is the acceleration due to gravity. To solve these two equations, SPH discretises a domain into a set of particles (or material points), each carrying material properties such as density, stress, velocity, and so on. The value of a function can be approximated using the SPH kernel approximation of a field function, $\mathbf{f}(\mathbf{x})$:

$$\mathbf{f}(\mathbf{x}) = \int_{\Omega} \mathbf{f}(\mathbf{x}') W(\mathbf{x} - \mathbf{x}', h) d\mathbf{x}', \quad (3)$$

where $W(\mathbf{x} - \mathbf{x}', h)$ is the kernel function; h is the smoothing length such that $W = 0$ for $|\mathbf{x} - \mathbf{x}'| > kh$ where κ is a constant that together with h , defines the radius of the support domain of the kernel function at position \mathbf{x} . From herein, $W(\mathbf{x} - \mathbf{x}', h)$ is written as W_{ij} which represents the value of the kernel function using the positions of particles i and j . The choice of kernel here is the Wendland C2 kernel, which usually requires a larger kernel radius compared to other kernel functions such as the cubic spline, but benefits from reduced pairing instability [54]:

$$W_{ij} = \frac{\alpha_d}{h^3} \left(1 - \frac{q}{h}\right)^4 (2q + 1), \quad (4)$$

where $\alpha_d = \frac{21}{16\pi}$ in three spatial dimensions; and $q = \frac{r_{ij}}{h}$. For the Wendland C2 kernel, with $\kappa = 2$, we find that good results are obtained for $1.5 \Delta x \leq h \leq 2.0 \Delta x$, where Δx is the initial particle spacing. In this work, we adopt $h = 1.75 \Delta x$. Using this kernel function, we can then discretise Eq. (3) and its spatial gradient as:

$$\mathbf{f}(\mathbf{x}_i) = \sum_j \frac{m_j}{\rho_j} \mathbf{f}(\mathbf{x}_j) W_{ij}, \quad (5)$$

$$\nabla \mathbf{f}(\mathbf{x}_i) = \sum_j \frac{m_j}{\rho_j} \mathbf{f}_{ij} \nabla^T W_{ij}, \quad (6)$$

where $\mathbf{f}_{ij} = \mathbf{f}(\mathbf{x}_i) - \mathbf{f}(\mathbf{x}_j)$. Using Eqs. (5–6), Eqs. (1–2) can be discretised as:

$$\frac{D\rho_i}{Dt} = \rho_i \sum_j \frac{m_j}{\rho_j} \mathbf{v}_{ij} \cdot \nabla W_{ij}. \quad (7)$$

$$\frac{D\mathbf{v}_i}{Dt} = \sum_j m_j \left(\frac{\boldsymbol{\sigma}_i}{\rho_i^2} + \frac{\boldsymbol{\sigma}_j}{\rho_j^2} \right) \cdot \nabla W_{ij} + \mathbf{g} \quad (8)$$

The above equations alone usually result in significant pressure fluctuations in the simulation that render the simulation unstable or inaccurate. To stabilise the numerical solution, we use the artificial viscosity [23] and density diffusion [55] terms. The density diffusion serves to smoothen the pressure profile, which ensures the accuracy of the evaluation of the pressure-dependant shear stress tensor. Introducing artificial viscosity and density diffusion, Eqs. (7–8) become:

$$\frac{D\rho_i}{Dt} = \rho_i \sum_j \frac{m_j}{\rho_j} \mathbf{v}_{ij} \cdot \nabla W_{ij} + \delta h c \sum_j \frac{m_j}{\rho_j} \Psi_{ij} \cdot \nabla W_{ij}, \quad (9)$$

$$\frac{Dv_i}{Dt} = \sum_j m_j \left(\frac{\sigma_i}{\rho_i^2} + \frac{\sigma_j}{\rho_j^2} \right) \cdot \nabla W_{ij} + \mathbf{g} + \alpha_\pi h c \rho_0 \sum_j \frac{m_j}{\rho_i \rho_j} \frac{\mathbf{v}_{ij} \cdot \mathbf{x}_{ji}}{|\mathbf{x}_{ij}|} \nabla W_{ij} \quad (10)$$

where c is the speed of sound in the material; ρ_0 is the reference density of the material; and δ and α_π are constants and are selected as 0.1 [55] and 0.04, respectively. $\langle \cdot \rangle$ is the Macaulay brackets, which prevents the artificial viscosity term behaving as a real viscosity and ensures it serves only to stabilise the numerical scheme; and Ψ_{ij} is calculated as:

$$\Psi_{ij} = 2\rho_{ji} \frac{\mathbf{x}_{ji}}{|\mathbf{x}_{ji}|^2} - [\langle \nabla \rho \rangle_i^L + \langle \nabla \rho \rangle_j^L] \quad (11)$$

$$\langle \nabla \rho \rangle_a^L = \sum_b \rho_{ba} \mathbf{L}_a \nabla W_{ab} \frac{m_b}{\rho_b}, \quad (12)$$

$$\mathbf{L}_a = \left[\sum_b \mathbf{x}_{ba} \otimes \nabla W_{ab} \frac{m_b}{\rho_b} \right]^{-1} \quad (13)$$

where \mathbf{L} is the gradient renormalisation matrix [56] and $\nabla \rho^L$ is the renormalised density gradient.

2.2 Rheological model

A formulation of the Cauchy stress tensor is required to close Eqs. (9–10). When modelling granular materials in SPH the most common approaches of formulating the stress tensor is to treat the material as an elasto-plastic solid [25, 31, 40, 57], or a visco-plastic fluid [41]. The latter approach is commonly used when aiming to capture the fluid-like behaviour of granular material. Because the applications here rely heavily on the fluid-like behaviour of granular material, we adopt a visco-plastic approach to modelling the granular material. Accordingly, the stress tensor for particle i is written as

$$\boldsymbol{\sigma}_i = -p_i \mathbf{I} + \boldsymbol{\tau}_i, \quad (14)$$

where p_i is the isotropic pressure for particle i ; \mathbf{I} is the identity tensor; and $\boldsymbol{\tau}_i$ is the shear stress tensor for particle i . Here, like in the classical weakly compressible SPH [23], we use an equation of state to determine the pressure:

$$p_i = c^2 (\rho_i - \rho_0), \quad (15)$$

where c is the speed of sound, which is assumed to be $10 v_{\max}$ [23]. As for the shear stress tensor, when considering granular material in its fluid regime, it is common to treat it as a non-Newtonian Bingham fluid. In its one-dimensional form, the shear stress for a Bingham fluid is written as:

$$\tau = \eta_0 \dot{\gamma} + \tau_y \quad (16)$$

where η_0 is the dynamic viscosity, and τ_y is a yield stress. The model supposes that for shear stresses beneath τ_y , the material is rigid, and flow occurs when $\tau > \tau_y$. To incorporate the shear strength of granular materials, which is typically described as being pressure-dependent, we incorporate the Mohr–Coulomb yield criteria, which allows the yielding shear stress to be described as a function of pressure, as well as easily obtained material properties:

$$\tau_y = c + p \tan \phi, \quad (17)$$

where c is cohesion, and ϕ is the internal angle of friction. Substituting Eq. (17) into Eq. (16), we obtain the 1D modified Bingham shear stress:

$$\tau = \eta_0 \dot{\gamma} + c + p \tan \phi. \quad (18)$$

In previous applications of this model, the above modified Bingham model can be rewritten using an equivalent fluid viscosity, η , for use in Navier–Stokes solvers [58–60]:

$$\eta = \eta_0 + \frac{c + p \tan \phi}{\dot{\gamma}}. \quad (19)$$

As our simulations are in 3D, we use the generalised form of the modified Bingham shear stress:

$$\boldsymbol{\tau}_i = \eta_0 \dot{\gamma}_i + (c + p \tan \phi) \frac{\dot{\gamma}_i}{\|\dot{\gamma}\|}, \quad (20)$$

where $\|\dot{\gamma}\| = \sqrt{\frac{1}{2} \dot{\gamma} : \dot{\gamma}}$ is the second invariant of the deformation tensor. In this form, the material is intended to behave as a rigid body for $\|\boldsymbol{\tau}\| < c + p \tan \phi$. The above modified Bingham model can be thought of as a precursor to the $\mu(I)$ model, where the $\mu(I)$ model takes the dynamic viscosity, η_0 , and the cohesion, c , as 0; and also exchanges $\tan \phi$ for a scalar friction value that varies with the inertial number. Like in the $\mu(I)$ model, which has been shown to capture unsteady flows reasonably well [37, 48, 61], here, c and η_0 are taken as 0 and the selection for ϕ will be discussed in later sections. Typically, when using the Bingham model, either with a constant τ_y or pressure-dependant τ_y as used here, the equivalent viscosity is used (Eq. 19), so that shear forces are calculated using an approximation of the Laplacian operator, and therefore, calculated separately from pressure forces. In these scenarios, the tendency for the equivalent viscosity to diverge for a vanishing strain rate can induce unphysically large forces. This issue is typically minimised by capping the viscosity [59] or regularising the viscosity, such as in the Bingham–Papanastasiou model [62]. Here, however, we use Eq. 20, and it should be apparent that while η_i approaches infinity as $\dot{\gamma}$ approaches 0, every element of the tensor $\frac{\dot{\gamma}_i}{\dot{\gamma}}$ is ≤ 1 for any finite $\dot{\gamma}_i$ thus implying that $\boldsymbol{\tau}_i$ does not become large for a given $\tan(\phi)p_i$. For this reason, we find that regularisation

of the apparent viscosity is not necessary to ensure a stable numerical scheme.

2.3 Boundary conditions

There are different methods available in the literature to model fully fixed and free-slip boundary conditions in SPH. Usually, these involve fixed virtual particles [63–65], but there are also dynamically generated ghost particles and analytical methods [24]. The simplest method is to use the virtual boundary described in [23], which uses artificial repulsive forces to interact with the SPH particles. Another approach is to use the fixed virtual particles and an SPH interpolation procedure to determine appropriate field variable quantities for the virtual particles. In the current work, we use a combined virtual particle, ghost particle approach as described in [25], where the fixed virtual particles enforce the fully fixed velocity condition, and the free-slip boundary condition is enforced by the ghost particles. Also, we use a repulsive force boundary to prevent penetration into the ghost boundary like that described in [66]. The combined approach is shown in Fig. 2.

In particularly turbulent or dynamic flows such as impact onto structures, there may be some penetration of the real particles into the ghost particle boundary, which can be prevented using a repulsive boundary. In the SPH literature, this repulsive force is applied using particles and the force is applied only in the direction normal to the boundary surface so as to avoid inducing additional shear [66, 67]. Contrary to typical uses of this type of boundary, here the force is applied when a real SPH particle is within r_0 of the defined boundary, instead of being applied based on interaction with virtual particles. In our simulations, this

boundary is used only for the flume sidewalls. The repulsive boundary force vector, $\mathbf{f}_{b,i}$, is determined by

$$\mathbf{f}_{b,i} = D \left(\left(\frac{r_0}{|\mathbf{r}_n|} \right)^{p_1} - \left(\frac{r_0}{|\mathbf{r}_n|} \right)^{p_2} \right) \frac{\mathbf{r}_n}{|\mathbf{r}_n|^2}, \quad (21)$$

where \mathbf{r}_n is the vector between the boundary and particle i normal to the boundary, p_1 and p_2 are constants, chosen as 4 and 2, respectively, $D = c^2(m/s)^2$ is a constant controlling the magnitude of the force, and r_0 is the interaction cut-off distance where for $|\mathbf{r}_n| \geq r_0$, $\mathbf{f}_{b,i} = 0$. Here, we choose $r_0 = \Delta x/4$ instead of $r_0 = \Delta x/2$ typically used [66, 67] to reduce the influence the boundary on the simulation results.

2.4 Time-integration scheme

With the spatial discretisation being described by SPH, the discretisation of the time-integration is required for the integration of Eqs. (1–2). Here, we use the second-order accurate Leap-Frog (LF) time-integration scheme, which is sufficiently stable, accurate, and fast due to only requiring one calculation of forces for each timestep [68]. In the LF scheme, the density and velocity are calculated at mid-increments, whereas the position is updated at full-increments. Note that stress is a function of strain rate and pressure (and therefore density), so it is calculated at the mid-increment when calculating forces. For a given timestep, the density and velocity are brought forward to the mid-increment using material derivatives from the previous timestep (if available):

$$\rho_{n+\frac{1}{2}} = \rho_n + \frac{\Delta t}{2} \left(\frac{D\rho}{Dt} \right)_{n-1}, \quad (22)$$

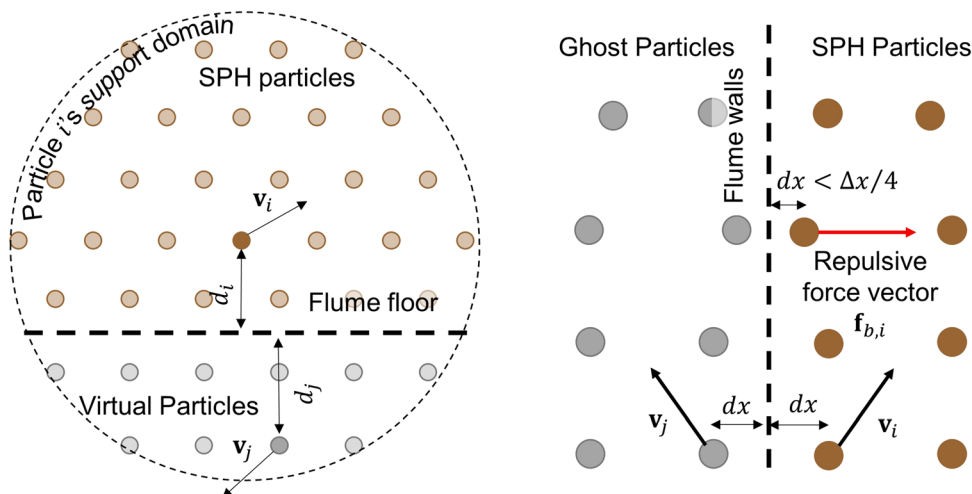


Fig. 2 Illustration of the Boundary conditions being used. Left: virtual particle approach of enforcing zero-velocity boundary, right: ghost particle approach to enforce reflective boundary, supported by the anti-penetration repulsive boundary

$$\mathbf{v}_{n+\frac{1}{2}} = \mathbf{v}_n + \frac{\Delta t}{2} \left(\frac{D\mathbf{v}}{Dt} \right)_{n-1}, \quad (23)$$

Here, the material derivatives are calculated (i.e. $(\frac{D\rho}{Dt})_n$, $(\frac{D\mathbf{v}}{Dt})_n$), and then position, density, and velocity can be updated to the full-increment according to:

$$\rho_{n+1} = \rho_n + \Delta t \left(\frac{D\rho}{Dt} \right)_n, \quad (24)$$

$$\mathbf{v}_{n+1} = \mathbf{v}_n + \Delta t \left(\frac{D\mathbf{v}}{Dt} \right)_n, \quad (25)$$

$$\mathbf{x}_{n+1} = \mathbf{x}_n + \Delta t \times \mathbf{v}_n. \quad (26)$$

The size of Δt is determined using the Courant–Friedrichs–Lowy (CFL) stability condition, which, for SPH states that

$$\Delta t = C_{CFL} \frac{h}{c} \quad (27)$$

where a suitable value for C_{CFL} was found to be 0.2, which is used throughout the entirety of this paper. As stated earlier, the smoothing length, $h = 1.75\Delta x$, and the speed of sound, $c = 10 v_{\max}$, where v_{\max} is the maximum speed of the material in the simulation.

2.5 Particle shifting technique (PST)

In granular flows past rigid obstructions, the flow can exhibit a variety of behaviours such as bow shocks and granular vacuums [69]. In the context of water flowing past rigid obstructions, it has been shown that problems such as tensile instability and poor particle arrangement can inhibit SPH's ability to capture the vacuous region behind the obstruction. While there are a few approaches available aimed at regularising particle arrangements such as XSPH [70], the artificial stress method [71], and particle shifting approaches [72–74], we use the particle shifting technique described in [73], which has been shown to improve flows past obstructions to great effect. The approach is a modified version of the particle shifting technique described in [72], which itself is a combination of the artificial stress method of preventing tensile instability [71], and an early version of the particle shifting technique [75]. At the end of each timestep, the particle positions are shifted by a vector $\delta\mathbf{r}_i$, which depends on the arrangement of particles:

$$\begin{aligned} \delta\mathbf{r}_i = & -\frac{\Delta t \cdot v_{\max}}{h} (2h)^2 \\ & \cdot \sum_j \left(1 + 0.2 \left(\frac{W_{ij}}{W(\Delta x)} \right)^4 \right) \nabla W_{ij} \frac{m_j}{\rho_i + \rho_j} \frac{-b \pm \sqrt{b^2 - 4ac}}{2a}. \end{aligned} \quad (28)$$

where $\frac{\Delta t \cdot v_{\max}}{h} (2h)^2$ controls the magnitude of shifting,

ensuring that the shift is not too large and vanishes for a vanishing smoothing length. The ratio $\frac{W_{ij}}{W(\Delta x)}$ ensures that the shifting intensity grows as particles approach each other, and the direction of the shifting vector is based on the property of the vector $-\sum_j \nabla W_{ij}$ pointing in the direction of ‘emptiest space’ [76]. When shifting a particle with $\delta\mathbf{r}$, the field quantities are updated also, according to

$$\delta\varphi_i = \delta\mathbf{r} \cdot (\nabla\varphi)_i \approx \delta\mathbf{r} \cdot \sum_j \varphi_{ji} \nabla W_{ij} \frac{m_j}{\rho_j} \quad (29)$$

where φ is representative of the field variables ρ and \mathbf{v} . To summarise, the particle shifting requires the update of position, density, and velocity at the end of every timestep according to

$$\mathbf{x}'_i = \mathbf{x}_i + \delta\mathbf{r}_i, \quad (30)$$

$$\rho'_i = \rho_i + \delta\rho_i, \quad (31)$$

$$\mathbf{v}'_i = \mathbf{v}_i + \delta\mathbf{v}_i. \quad (32)$$

For free-surface SPH particles, the shifting vector, $\delta\mathbf{r}$, will shift the particles into empty space, causing a significant and unphysical spreading of particles. In the literature, for particles near the free-surface, the shifting vector is modified such that the component of the shifting vector normal to the free surface plays a lesser or no role in shifting [72, 73]. While these approaches of implementing the PST show good results, we find that the implementation of the PST in this numerical framework results in augmentation of the kinematics. Thus, we apply the PST less broadly, which is controlled by the parameter:

$$\tilde{W}_i = \sum_j W_{ij} \frac{m_j}{\rho_j}, \quad (33)$$

where for \tilde{W}_i less than a particular value, the PST shifting vector is not applied to particle i . We find that if the threshold for \tilde{W}_i is too low and the PST is applied too broadly, the flows tend to be accelerated significantly. To reduce this effect, the \tilde{W}_i threshold is chosen to be 0.8, where particles possessing \tilde{W}_i values beneath this do not have any shifting applied.

2.6 Parallel scheme

When studying the impact of granular flows on objects, the scale of the obstructions being considered is relatively small relative to the overall size of the simulated domain. This requires a high particle resolution (i.e. large number of particles), which can be time-consuming to the point of being impractical for a serial program. To overcome this issue, the parallel code described in [48] is used here, which uses the MPI communication standard to parallelise

the SPH program, and is aimed at CPU clusters with thousands of CPU cores. The parallel scheme uses the orthogonal recursive bisection (ORB) algorithm to subdivide the computational domain into coaxial boxes to be distributed amongst CPU cores. Following the distribution of particles, halo particle information is exchanged between cores to ensure that particles located on one core have the appropriate neighbouring particle information to conduct the relevant interpolations in the relevant equations. In each timestep, the exchange of real and halo SPH particles occurs at the mid-timestep—immediately before when the particle interaction list is generated, and forces are calculated for that timestep. The renormalised density gradient required in the density diffusion term in Eq. (11–13) and the stress tensor needed in calculating the forces in Eq. (10) are calculated after the interaction list is updated. Once the stress tensor and renormalised density gradient for each real particle are updated, they are exchanged between CPU cores to update each others' halo particles. Figure 3 shows a high-level flowchart describing the steps in the parallel algorithm within the overall time-integration scheme. Here, up to 3.8 million real SPH particles and over 800 thousand virtual boundary SPH particles are simulated when conducting simulations up to 192 CPU cores. All simulations are run either on NCI-Gadi or Pawsey Magnus, which, respectively, use nodes consisting of 2 Intel Xeon Platinum 8274 (Cascade Lake) CPUs (48 cores per node),

and nodes consisting of 2 Intel Xeon E5-2690V3 (Haswell) CPUs (24 cores per node).

3 Calibration and validation

Prior to investigating the interaction between granular flows and baffles, we need to calibrate and validate the numerical framework to match conditions produced in the physical experiment. To accomplish this, we use two test cases from [51], the first case is flow down without any baffles, and the second is flow impeded by an array of baffles. The first case is used to calibrate the friction angle as well as the container depth, and then the second case is used as validation of the calibrated parameters. The latter test case corresponds to the test with identification number H15_R3_L10_T30 from [51]. This test consists of three rows of baffles; each row spaced 100 mm apart (the first row being located at 800 mm downstream of the container gate). Each row consists of 30% transverse blockage using baffles 120 mm tall and 20 mm wide. The baffles are arranged in a staggered pattern, as illustrated in Fig. 4. In the experiment, a 100 kg mass of sand with an internal friction angle of 30°–32° packed to a bulk density of 1680 kg/m³ is initially held in a rectangular containment box. At the start of the experiment, a door on the containment box swings open, allowing the granular material

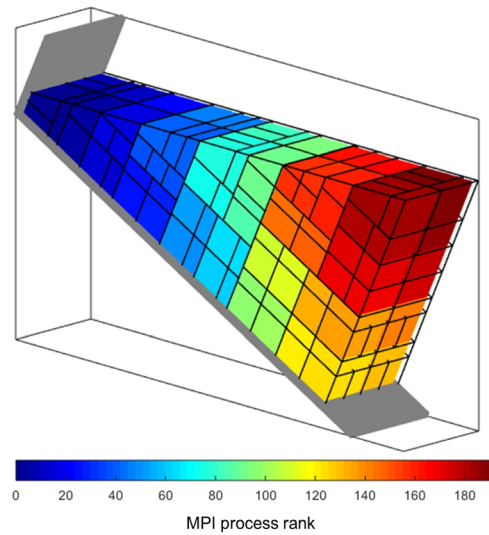
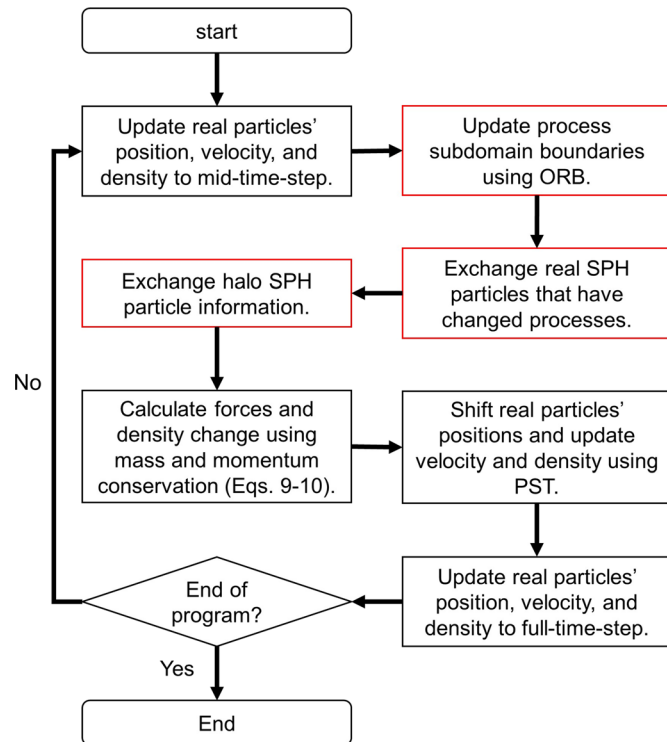


Fig. 3 Flowchart of the time-integration of SPH particles motions with a parallel scheme (left) and illustration of the ORB partitioning algorithm, subdividing the domain on 192 CPU cores (right)

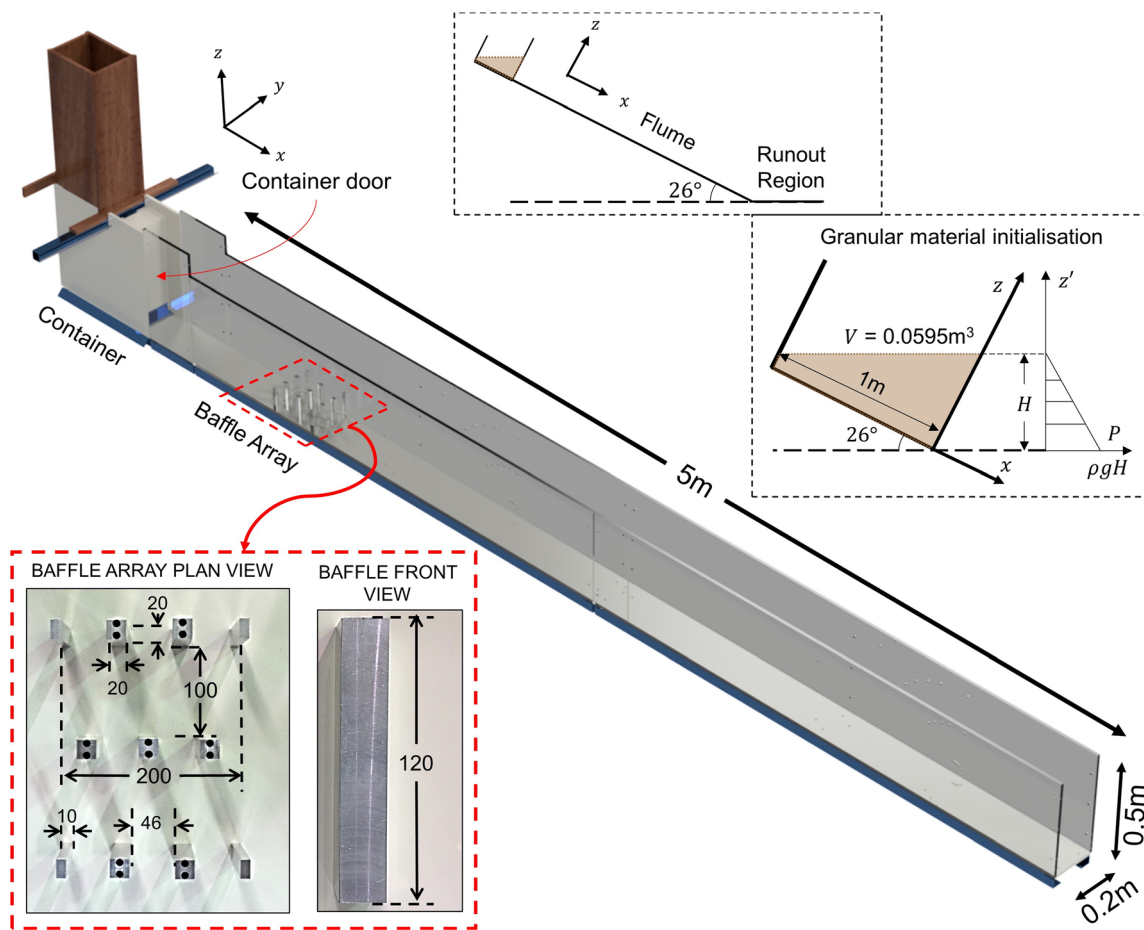


Fig. 4 Flume testing geometry, set-up, and initial conditions for the simulated granular material

to flow down a flume 5 m long, 0.2 m wide, and 0.5 m tall, and inclined at an angle of 26° to the horizontal. At the end of the flume is a ‘run-out region’ where the flume becomes horizontal. In the experimental work, the flow depth at 0.8 m downstream of the container gate is measured over time using a high-speed camera and the final distances in the run-out region are measured. The final flume geometry is shown in Fig. 4. The simulation set-up uses virtual particles to enforce the fully fixed velocity boundary condition on the flume floor, and the free-slip velocity boundary conditions are enforced on the flume walls, which is supported by a repulsive boundary condition to ensure no particle penetration occurs. The Cartesian coordinate system is rotated such that axes align with the flume geometry and the gravitational acceleration vector is modified accordingly. The granular material initial geometry is trapezoidal, so that the surface is horizontal. Additionally, the initial stress state in the granular material is assumed to be hydrostatic. The initial particle spacing is $\Delta x = 2.5$ mm, which equates to roughly 3.8 million SPH particles required to occupy the volume of 0.0595m^3 arranged on a square lattice aligned with the coordinate

system. The speed of sound used in the remainder of this paper is $c = 35$ m/s, which is approximately the maximum speed observed for the simulations conducted here.

The reported measurements of upstream flow depth and run-out distances from both test cases are used to calibrate the friction angle. The flow depth is measured at 0.8 m downstream of the container gate. We found that a more appropriate friction angle was found to be within the range of 26°–29°, which provides reasonable agreements between SPH simulations and experiments. Figure 5 shows the upstream flow depth and final run-out distances obtained for these various friction angles (i.e. 26°–29°). For all values, peak upstream flow depth was found to be very similar and matched the experimental data well. However, beyond 2 s after the flow front reaches the measurement point, the flow depth varies significantly with friction angle. For example, using an internal friction angle of 29° causes the granular material to accumulate upstream, causing an increase in upstream flow depth. In contrast, for an internal friction angle of 26°, flow continues for a long duration, transporting more material downstream. Overall, values between 27° and 28° produced reasonable

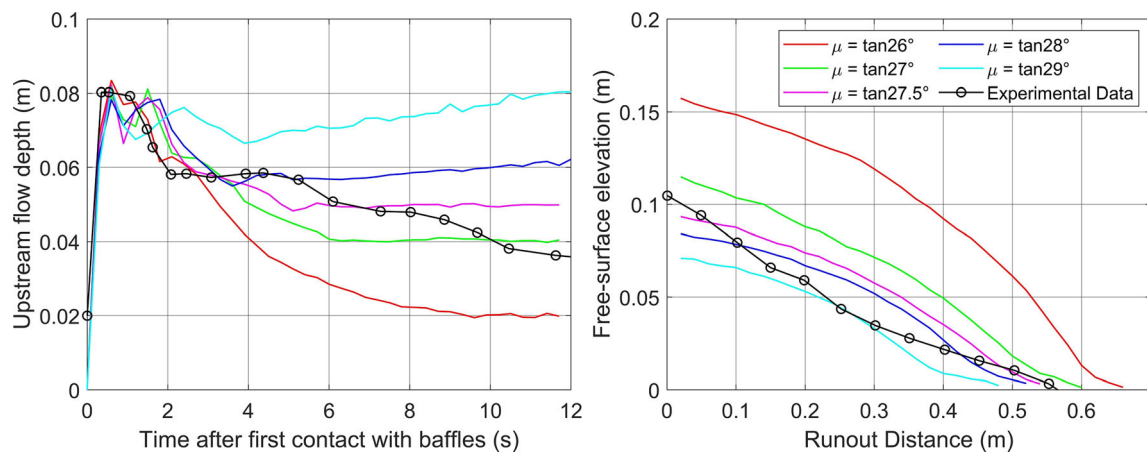


Fig. 5 The variation of upstream flow depth (left) and final run-out distance (right) with different internal friction angles

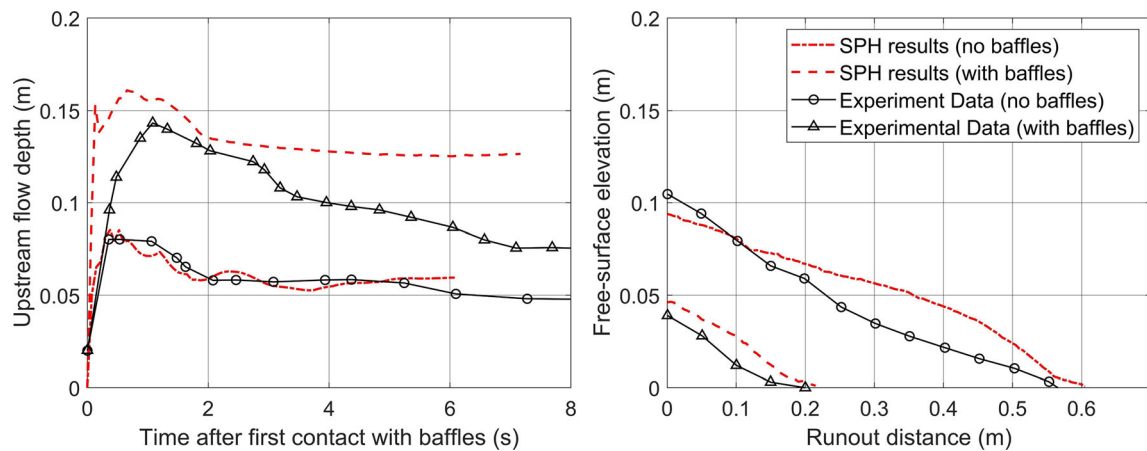


Fig. 6 Validation of SPH using upstream depths and final run-outs of experimental data with and without baffles

agreements. We opt to use an internal friction angle of 27.5° , which is used from here on.

Figure 6 shows the SPH simulations conducted using the calibrated friction angle for both flows with and without baffles, and the comparison to the measurements from the physical experiment. Considering the upstream flow depth, the agreement between the simulations and physical experiment for the case without baffles is good due to the calibration of the friction angle. When the flow front reaches the flow depth measurement point, the frontal velocity is 3.1 m/s, corresponding to a Froude number of 3.65. When introducing the baffles, the SPH simulations predict a sharp increase upstream flow depth after the flow front first impacts with the baffles, before decreasing slightly. This ‘kink’ in the curve can be attributed to granular material being ejected slightly upward at first impact, which was included in the measurements of the SPH results. The flow depth then increases more gradually to a global peak, and then slowly decreases until the flows reach a quasi-static state. While the SPH simulations

successfully capture an increase in overall upstream flow depth when compared to without baffles, it is apparent that the simulations over-predict the upstream flow-depth in comparison with the physical experimental data. This could be due to the difference in friction between the sand and flume walls, which was reported to be 21.8° , lower than the internal friction. This difference is not accounted for in the boundary conditions used in the simulations here and only partially compensated for in the calibration. But in terms of run-out distances, good agreement is obtained between the SPH simulations and experiments, with only a slight overestimation. However, there is an overestimation of volume that reaches the run-out region. Despite this, we conclude that reasonable agreement is obtained between the SPH simulations and the physical experiments.

4 Analysis and applications

4.1 Kinematics of flows through baffles

In the context of channelised flows, baffles are used to decelerate debris flows and minimise run-out distances or impact forces on other control structures downstream of the dam. Here, we describe the overall behaviour of the flow through the baffles as time progresses and compare them to flows without baffles, as shown in Fig. 7. For flows without baffles, the inclination of the flume results in a flow front that accelerates as it travels down the flume. The baffles disrupt the flow front, reducing the frontal velocity significantly, so that the flow front travels at less than 1.5 m/s when it first exits the baffle array, compared to over 3.5 m/s when unobstructed by baffles. After flowing through the baffle array, the flow front accelerates until it reaches the run-out region. For both flows with and without baffles, the flow front travels a short distance before coming to a complete stop, forming the final run-out. Subsequently, a granular jump is formed that propagates upstream. In the baffle array, material continues to slowly feed through the array long after the final run-out is obtained, albeit at a very low flow rate. While the flow without baffles reaches a static state after approximately 5.5 s of in-simulation time, the flow through baffles continues even after 7.5 s of in-simulation time. As for the flow front impact with the baffles, Fig. 8 shows the interaction of the flow front and the array of baffles over time, alongside shots taken from a high-speed video of the physical experiment. We note that the snapshots are taken from a video taken from a high-speed camera, and the time in the video when the granular material was released was not recorded. The simulation and experiment video are synced up based on a similar position in the flow-front (first row of shots in Fig. 9), and subsequent shots taken from the simulation and experiment video are the same time apart (i.e. 0.065 s after the first shot). As the flow front impacts the first row of baffles, a stagnation point develops immediately. Some of the material is ejected slightly upward due to the near-incompressible flow preventing lateral movement ($t = 0.460$ s). The portion of the flow-front that is not obstructed by the first row of baffles flows between the baffles, forming jets. Very shortly after the impact with the first row, the jets impact the second row and deflect at an angle. The deflected jets then join together to form jets that align with the final row of baffles ($t = 0.525$ s). Again, the final row of baffles deflects the granular material into the space between the baffles, which represents some of the outflows of the baffle array ($t = 0.591$ s). After the impact with the first row in the array of baffles, as the upstream flow depth increases, the jets between the first and second row of

baffles also increase in height and so does the material ejected upward by the first row of baffles. Shortly after the flow front impacts the baffle array, the jets between the first and second rows of baffles overtop the second row ($t = 0.591$ s) and then continue to flow unimpeded by the third row, initially creating two distinct outflow streams of granular material ($t = 0.66$ s). Without the impedance of the third row, this overflow maintains its speed. Eventually, it begins to accelerate to a speed of 2.4 m/s, before joining with the underflow, which is travelling at 1.7 m/s approximately ($t = 0.72$ s). This process is shown in Fig. 9. This overflow mechanism has been highlighted in [10, 51] to render the baffles less effective and should be minimised. The similarity between experimental observations and the simulation is relatively good. This is evidenced by the successful simulations of the jets that travel between rows of baffles and the overflow of granular material. However, the constitutive relations used here lack the means of capturing the granular material's transition to the granular gas phase that occurs shortly after impact with the baffles. Therefore, in the SPH simulations, no spreading of grains occurs due to impact of granular material with the baffles.

4.2 Preventing overflow using tall baffles

As shown above, and suggested by others [10, 51], the granular flow that travels over the array of baffles (i.e. overflow) reduces the effectiveness of the baffles and should be avoided. In [51], the effect of increasing the height of the baffles was shown to reduce run-out distances and minimise overflow. However, it is unclear to what height the baffles should be raised to prevent overflow altogether. While this may be time-consuming in physical experiments, it is straightforward for numerical simulations. Here, we investigate the difference in flow kinematics after increasing the baffle height substantially. To do so, we increase the baffle height from the previous 0.12 m to 0.25 m and observe the change in flow behaviour. Firstly, looking at upstream flow depth and final run-out distance (Fig. 10), the increased baffle height does much to reduce final run-out distances, from approximately 0.2 m in the SPH simulation to about 0.08 m, which is a significant relative reduction in run-out distances. The upstream flow depth shows a similar trend compared to the 0.12 m tall baffles. Still, the depth is approximately 0.05 m higher, implying greater volume retention and attenuation of flows in the early parts of the simulation. As time advances, the retained volume is released slowly downstream of the baffles. Final run-out distance is obtained at approximately $t = 4.4$ s. However, there is still motion near the array of baffles as the granular material upstream slowly flows through the baffle array and is released downstream. During the early stages of the flow impact

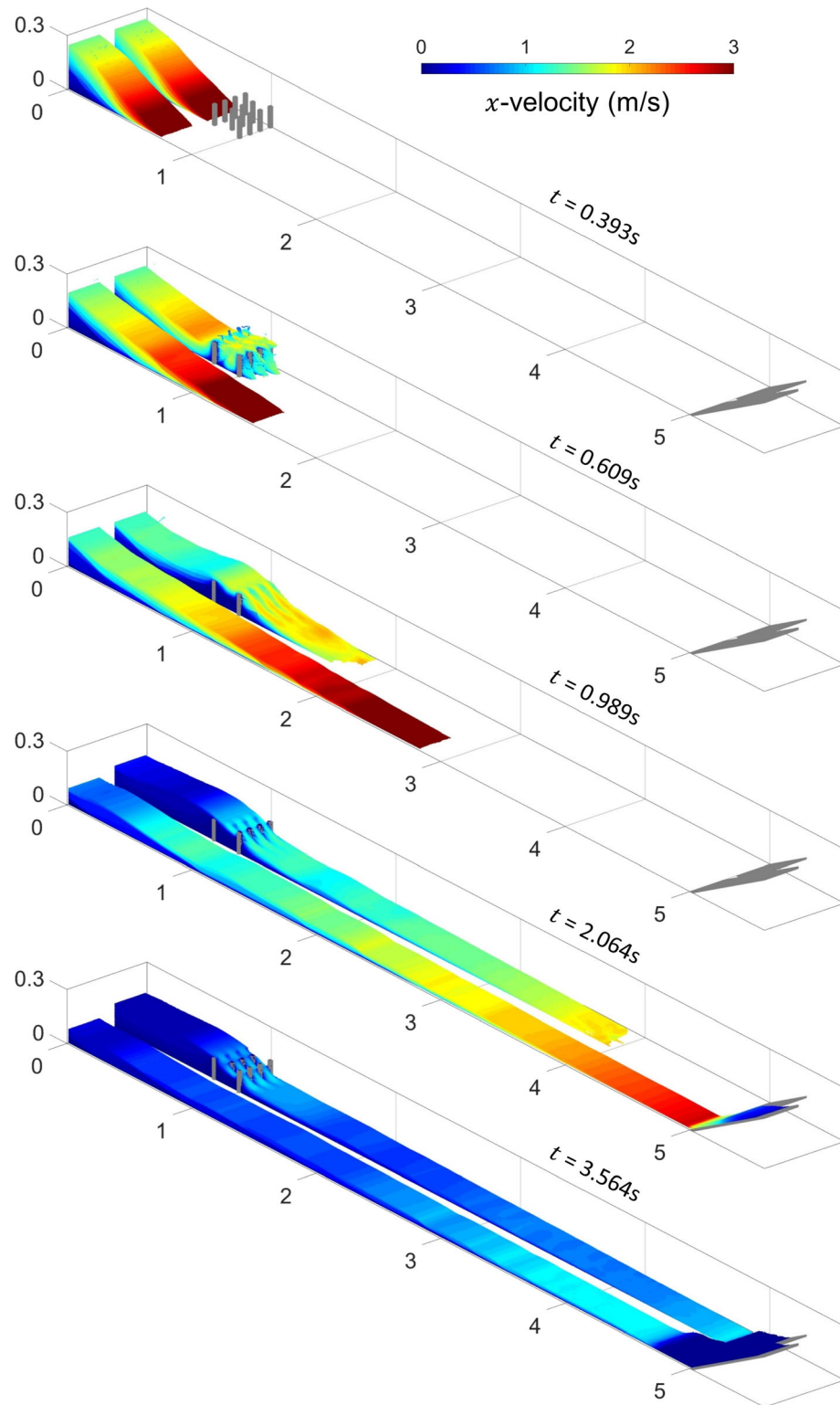


Fig. 7 Progression of granular flow down inclined flume with and without the obstruction of baffles

with the baffles, the flow kinematics do not differ much between the 0.12 m and 0.25 m tall baffles up to 0.53 s after the beginning of the simulation, which is when overflow begins to occur in the 0.12 m tall baffle array. In

the 0.25 m tall baffles the overflow is prevented entirely. Therefore, the only material flux downstream of the 0.25 m tall baffles is due to flow between baffles, unlike in the 0.12 m tall baffle array, where overtopping contributes to

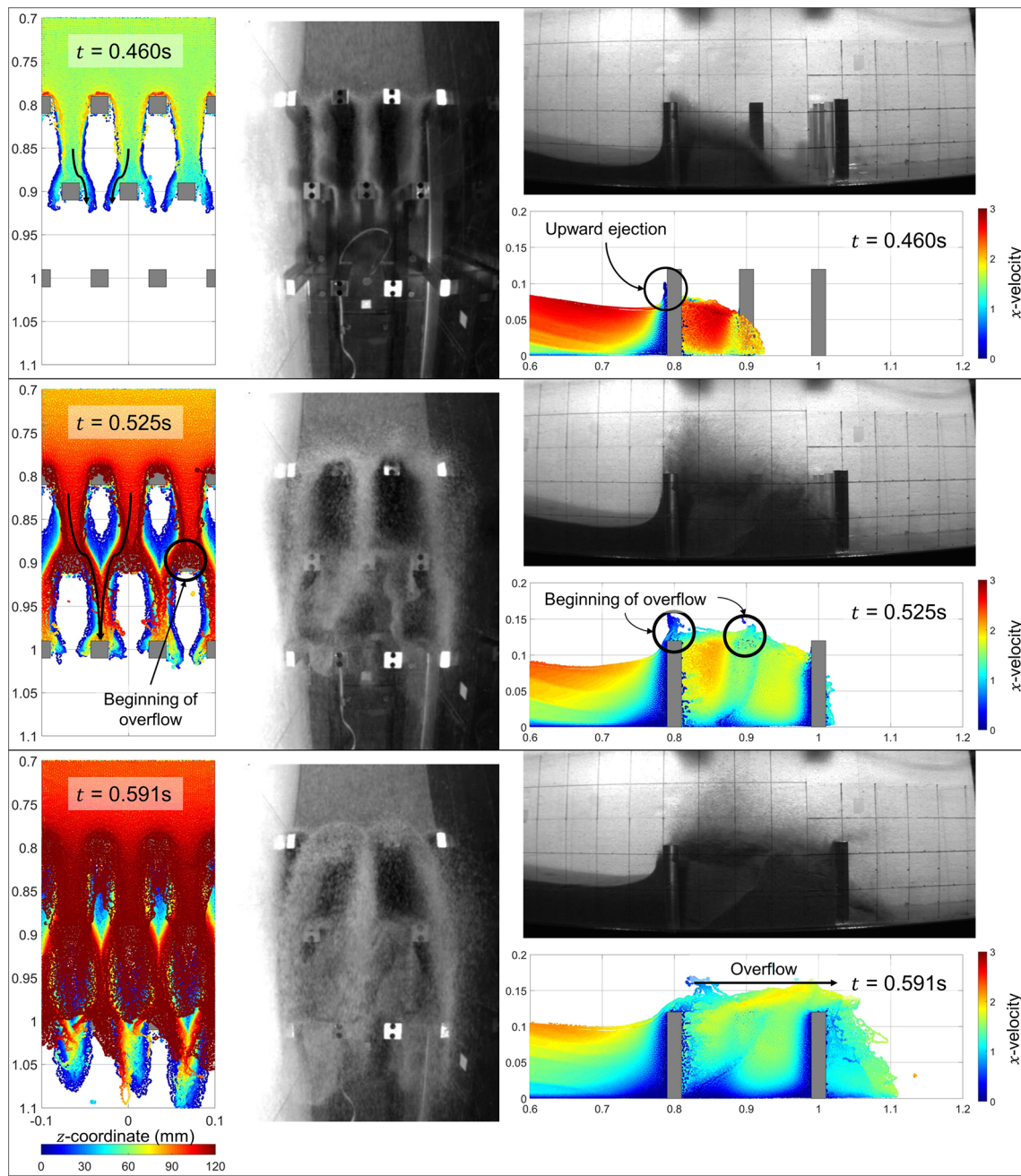


Fig. 8 Comparison of flow kinematics between experiment and SPH simulations

the flux as well (Fig. 11). The overflows of the baffle array have a clear consequence on flows, because, for both baffle heights, the flow between the baffles exits the baffle array at the same x -velocity (1.7–1.8 m/s), but in the case of the taller baffles, there is no overflow to accelerate the flow front. The maximum upstream depth measured using the tall baffles is 0.21 m, suggesting that to maximise baffles' capability to impede flows, they ought to be at least $0.21 / 0.08 = 2.63$ times the expected maximum flow depth of the debris flows without baffles. The results from the validation

conducted earlier would suggest that this conclusion is conservative.

4.3 Pressure acting on baffles

A key concern for engineers to design baffles is the peak forces or pressures acting on the baffles in addition to kinematics. While design standards exist for other flow control structures such as check dams [9], the pressure acting on baffles to impede granular flows are not

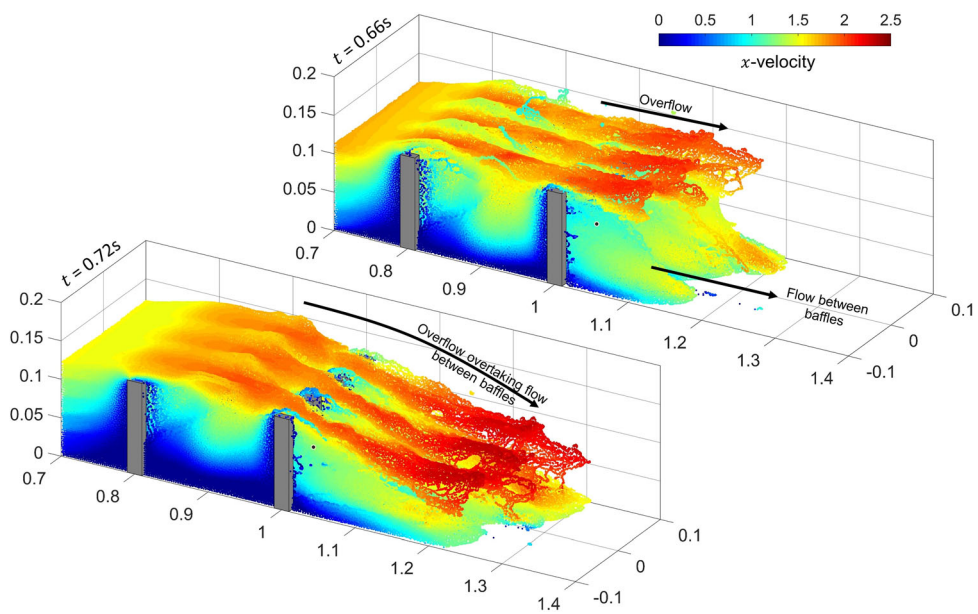


Fig. 9 Influence of overflow on outflow kinematics

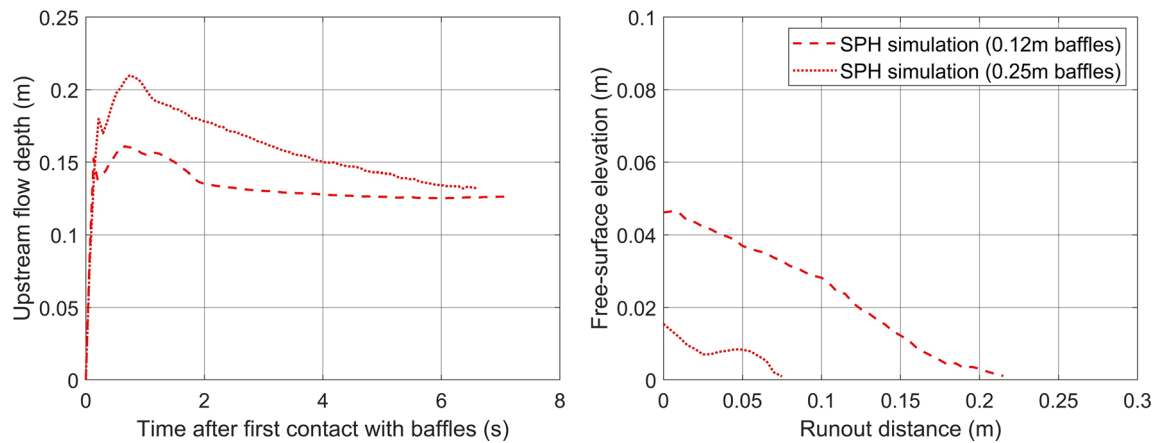


Fig. 10 Upstream flow depth and run-out distance between using 0.12 m and 0.25 m tall baffles

understood well. While in physical experimentation, measurement of dynamic data such as pressure and forces is not straightforward due to requiring high sampling rate, appropriate load cell selection, and influence of arching on measurement accuracy; in SPH, measurement of pressure can be relatively straightforward. To measure pressure, interpolation points are used which approximate a field quantity (in this case pressure) by performing a corrected SPH interpolation at a point (this process is described in [25]). Here, we place interpolation points along the vertical of the upstream face of the baffles not adjacent to the vertical boundary walls, using 10 equally spaced points per baffle along the height of the baffle. Figures 12 and 13 show the measured pressure at various points in time after the flow front first impacts the 0.12 m tall baffle array. In the early stages of the impact, high pressures develop

where the granular material impacts the baffles and low-pressure zones between the baffles where the flow passes through. The high-pressure zones propagate from the baffles slightly upstream in a fan-like pattern, reminiscent of the stress profile observed in soil arching in soil mechanics [77], or the silo/hopper discharge problem in granular flows [78], suggesting that arching likely plays a meaningful role in the attenuation of flows that travel between the baffles, which has also been proposed in the literature [79]. However, this could not be explored further here, as the constitutive relations used to simulate the granular flows are unable to capture the arching effect [48, 78] accurately. In terms of the flow along the height of the baffles, the pressure distributions required for design may be challenging to predict. In the pressure measurements taken here, we observe that the maximum pressure is experienced

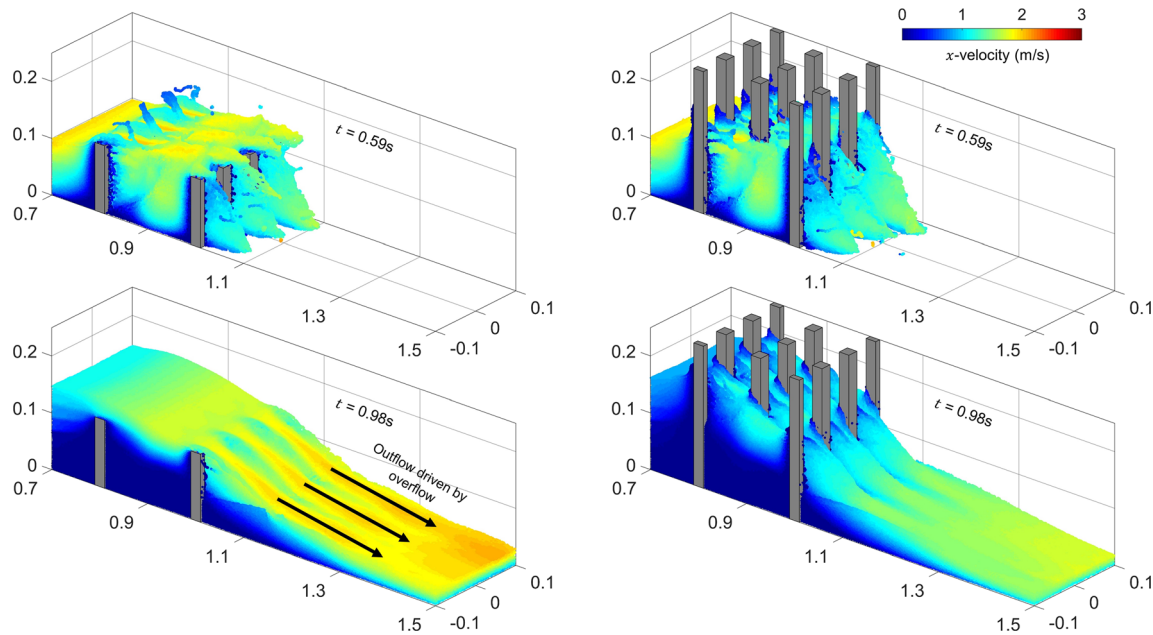


Fig. 11 Outflow kinematics of flow through 0.12 m (left) and 0.25 m (right) tall baffle arrays

by the first row of baffles with the second and third rows experiencing lower pressure throughout the entire flow process, and the third row experiencing the least. Shortly after impact, the pressure distribution in the first row of baffles resembles a statistical Fisher-Snedecor (F) distribution curve along the height of the baffle where the peak pressure at any given time occurs some distance above the base. We observe that peak pressures experienced by the first row of baffles are about 16 kPa, concentrated 0.02 m from the base of the flow and negative pressure is observed at the height where granular material is ejected upward. The occurrence of a small negative pressure is due to the flow ‘detaching’ from the top and sides of the baffles, which in the current weakly compressible SPH framework, results in decreased density, and therefore negative pressures due to the use of an Eq. (15) to relate density to pressure (i.e. equation of state). Unless a specific treatment is adopted (e.g. setting negative pressure to zero), this issue is unavoidable when adopting the standard weakly compressible SPH framework for fast flows impacting against structures, which often results in the surface-tension-like structures [80]. While this is unphysical for granular flows (though acceptable for debris flows), tensile pressures are small and only occurs on the free-surface where the flow detaches from the structures, and thus are commonly accepted in literature [80, 81]. As the upstream depth increases, more material is pressed against the first row of baffles. By using a lattice of pressure interpolation points along the upstream facing face of the baffle, a pressure distribution can be obtained, and with it an estimation of the pressure forces acting on the baffle over time. These

force measurements are shown in Fig. 14, which also includes the force measurements on the 0.25 m tall baffles. For the 0.12 m tall baffles, we observe that the peak force does not correspond to the moment of impact, but a short time after impact, suggesting that design of baffles requires the consideration of material pileup in addition to dynamic pressure like how check dams are designed [82, 83]. This is further exemplified with the forces acting on the 0.25 m tall baffles. The maximum force of 13.6 N experienced by a 0.25 m tall baffle is found to be largely due to the pileup of material upstream of the baffle array, instead of impact forces. In comparison, the maximum force on the 0.12 m tall baffle is 10.9 N. For comparison with design recommendations, we use the method to estimate debris flow impact load on rigid barriers from [82]:

$$F = \alpha \rho v^2 \sin \beta h w \quad (34)$$

where F is the estimated impact load (N), α is the dynamic pressure coefficient, ρ is the density of debris flows, v is the debris velocity at impact, h is debris thickness, w is debris width, and β is the angle between impact face of barrier and debris motion. Here, we adopt $\beta = 90^\circ$, h is taken as 0.08 m, v as 3.2 m/s, ρ is 1680 kg/m³, and w of 0.02 m for an individual baffle. Reported range of α typically varies between 0.5 and 2.5, where 2.5 is recommended to include the impact of boulders [82]. This range of α corresponds to a range of impact forces between 13.8 N and 68.8 N. The SPH measured forces are slightly beneath this range due to non-uniform pressure along the baffle width in contrast with constant pressure along the width of a rigid barrier.

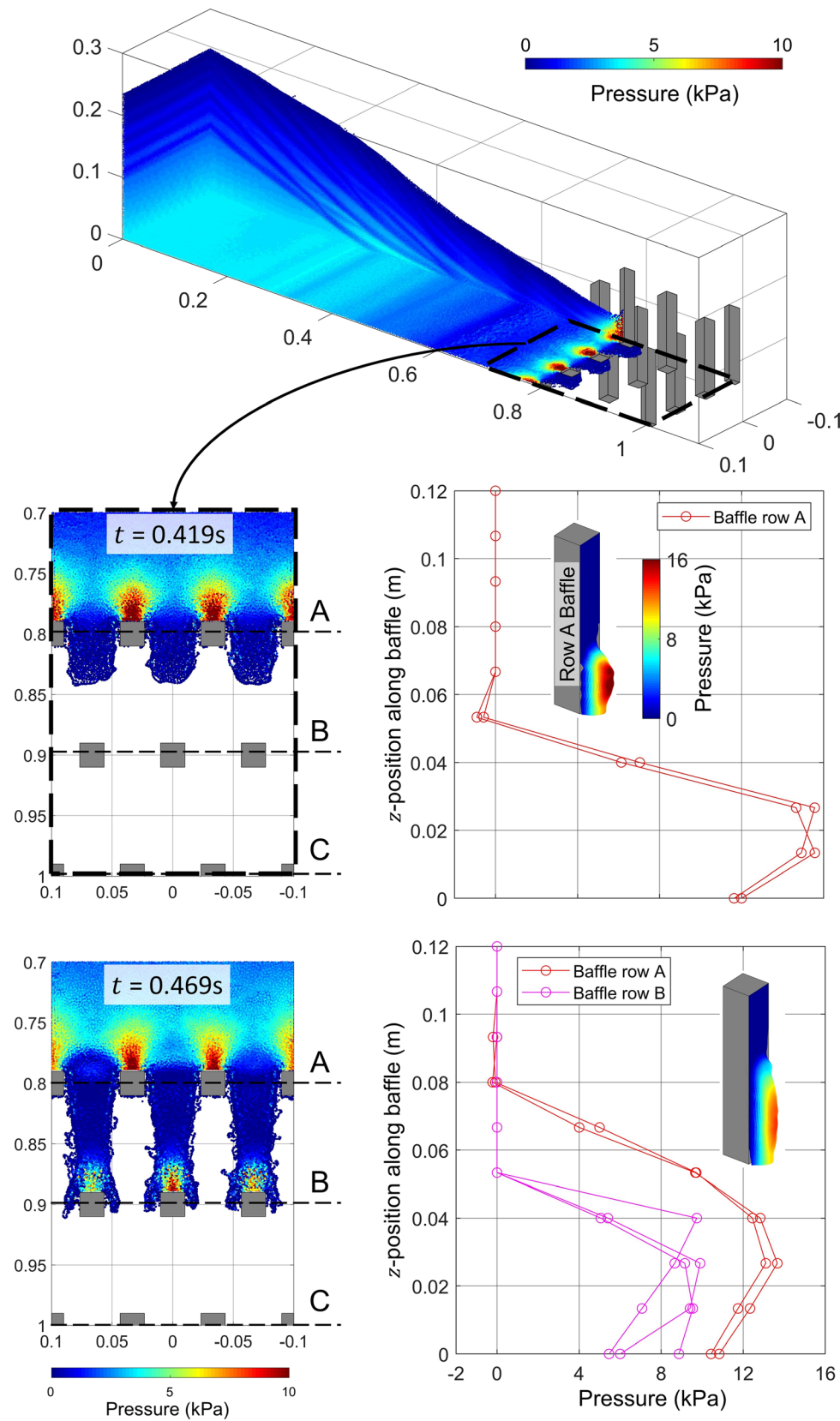


Fig. 12 Basal pressure profile and measured pressure along the height of each baffle as flow front travels through the baffle array

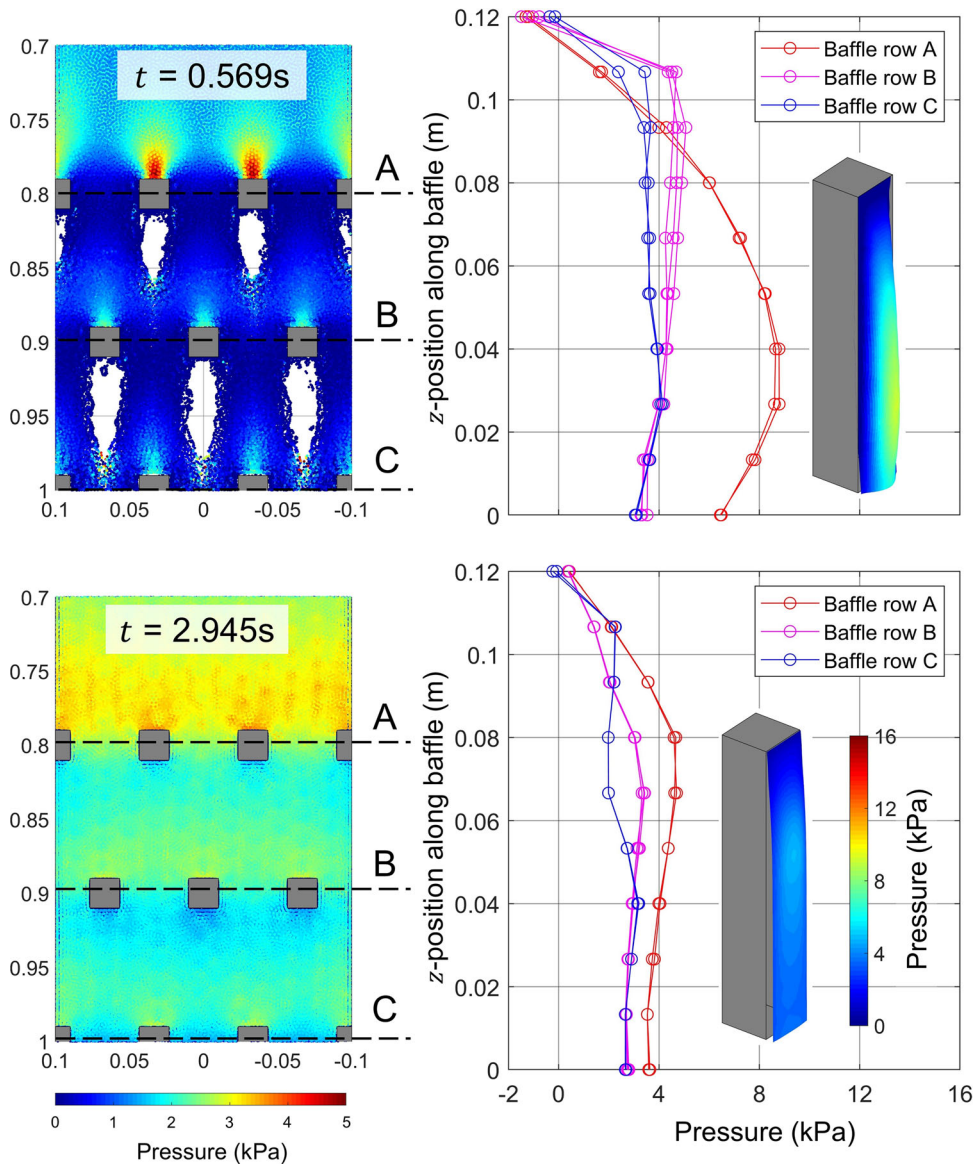


Fig. 13 Basal pressure profile and measured pressure along the height of each baffle as flows become static

4.4 Comparison of baffle performance with check dams

While baffles can be placed immediately in front of check dams to reduce the impact forces on the check dam, it is not uncommon to use multiple check dams in succession to delay flows. Still, the comparative performance of each approach has not been explored. Here, we investigate the comparative performance of a dual check-dam system. The first dam is placed 0.8 m downstream of the container gate (i.e. the same location as the first row of baffles). For comparison, the check dam is oriented in the same direction as the baffles (i.e. normal to the flume floor), and the same height and width are chosen (i.e. 120 mm tall and 80 mm wide), the height being similar to previous studies

[9]. The downstream distance the second check dam is placed is based on the recommendations by [84]:

$$L_{\min} = \frac{H}{(1-n)\tan\theta}, \quad (35)$$

where L_{\min} is the minimum distance between successive rigid barriers, n is a parameter based on the expected angle of debris deposition, H is the rigid obstruction height, and θ is the slope inclination. In the literature [82], appropriate n values are reported to vary between 1/6 and 3/4. Here we adopt $n = 3/4$, which results in a value for $L_{\min} = 0.66\text{ m}$. We, therefore, choose the downstream distance of the second check dam to be 0.7 m downstream of the first. Figure 15 shows the progression of flows for the check dam cases in comparison with the baffles for both 0.12 m

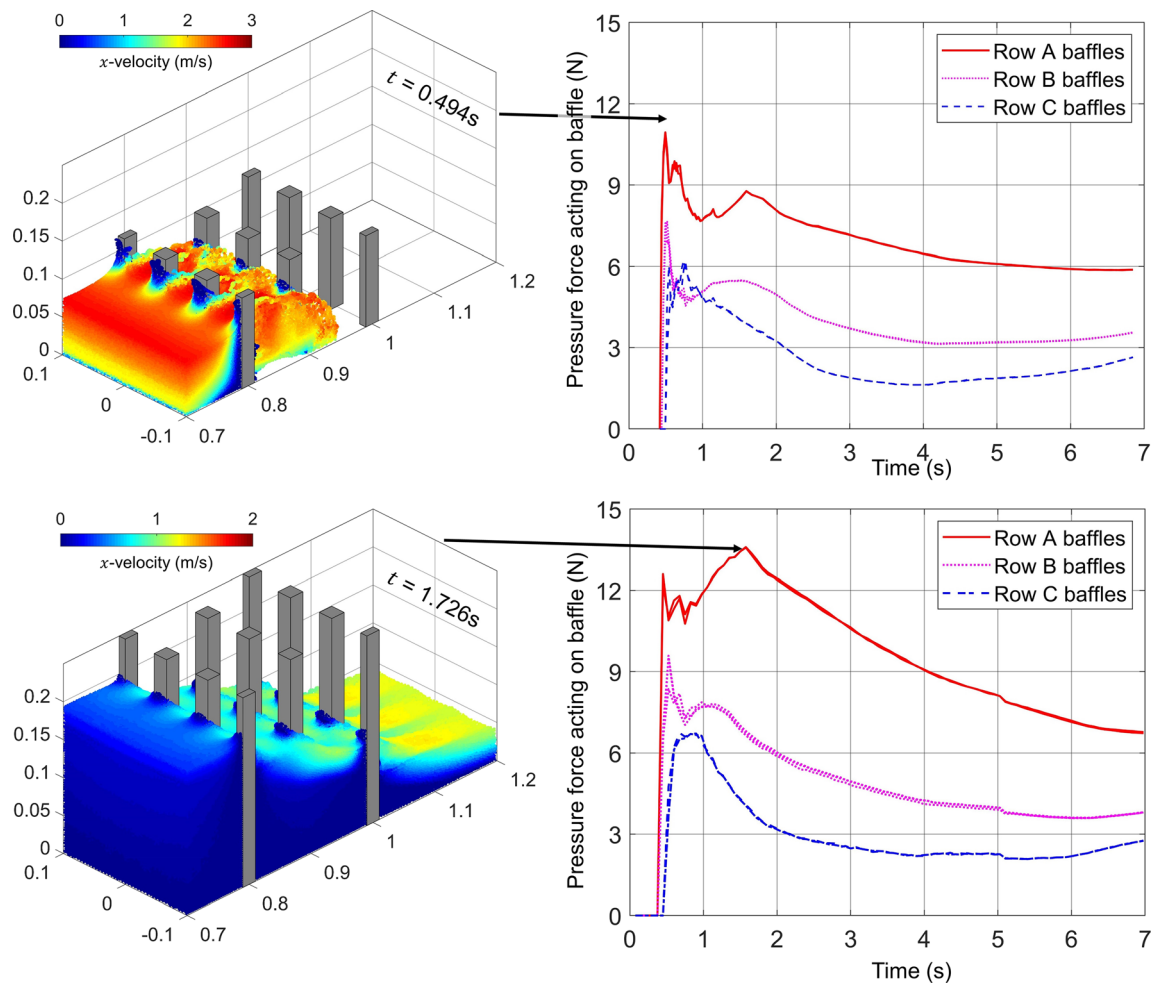


Fig. 14 Approximated force acting on each baffle and pressure distribution on baffles at the moment corresponding to peak force

and 0.25 m tall. The dual-barrier check dam system works very effectively in preventing the bulk of the material from reaching the run-out region. However, there is a small amount of overshoot that overcomes both dams and is able to accelerate and reach the run-out region. This is more visible in Fig. 16. Preventing this overshoot requires either taller dams or moving the second dam further downstream [9]. Comparing run-out distances show that the small overflow volume results in greater run-out distance compared to baffles, but with less volume of material travelling to the run-out region. But by making further small adjustments to the check dam heights and distances, the overflow could be prevented altogether, and no material would reach the run-out, implying that check dams are likely more effective in decelerating granular flows under purely channelised conditions. This performance also comes with the disadvantage of significantly large forces (Fig. 17). With a width of 0.2 m, Eq. 34 estimates maximum forces acting on the check dam to be between 137.6 N and 275.2 N, which the SPH measured forces of 177 N fall within. The forces that the entire dam

experiences are an order of magnitude larger than an individual baffle of the same height as the dam experiences approximately 177 N and a single 0.12 m tall baffle experiences approximately 11 N. Even after normalising for obstruction width (i.e. total force divided by obstruction width), the maximum force per unit-width experienced by the dam is approximately $177 \text{ N}/0.2 \text{ m} = 885 \text{ N/m}$. In contrast, an individual baffle with the same height will only experience approximately $11 \text{ N}/0.02 \text{ m} = 547 \text{ N/m}$. This would imply that while the ability of the check dams to reduce run-out is greater, it would come at a significantly higher cost to construct.

4.5 Measuring effectiveness of debris flow control structures

Primarily, the control structures considered here serve to minimise or prevent the damage to currently existing structures, or to reduce the impact on another control structure downstream. The mechanism by which this occurs has usually been explained as being due to either

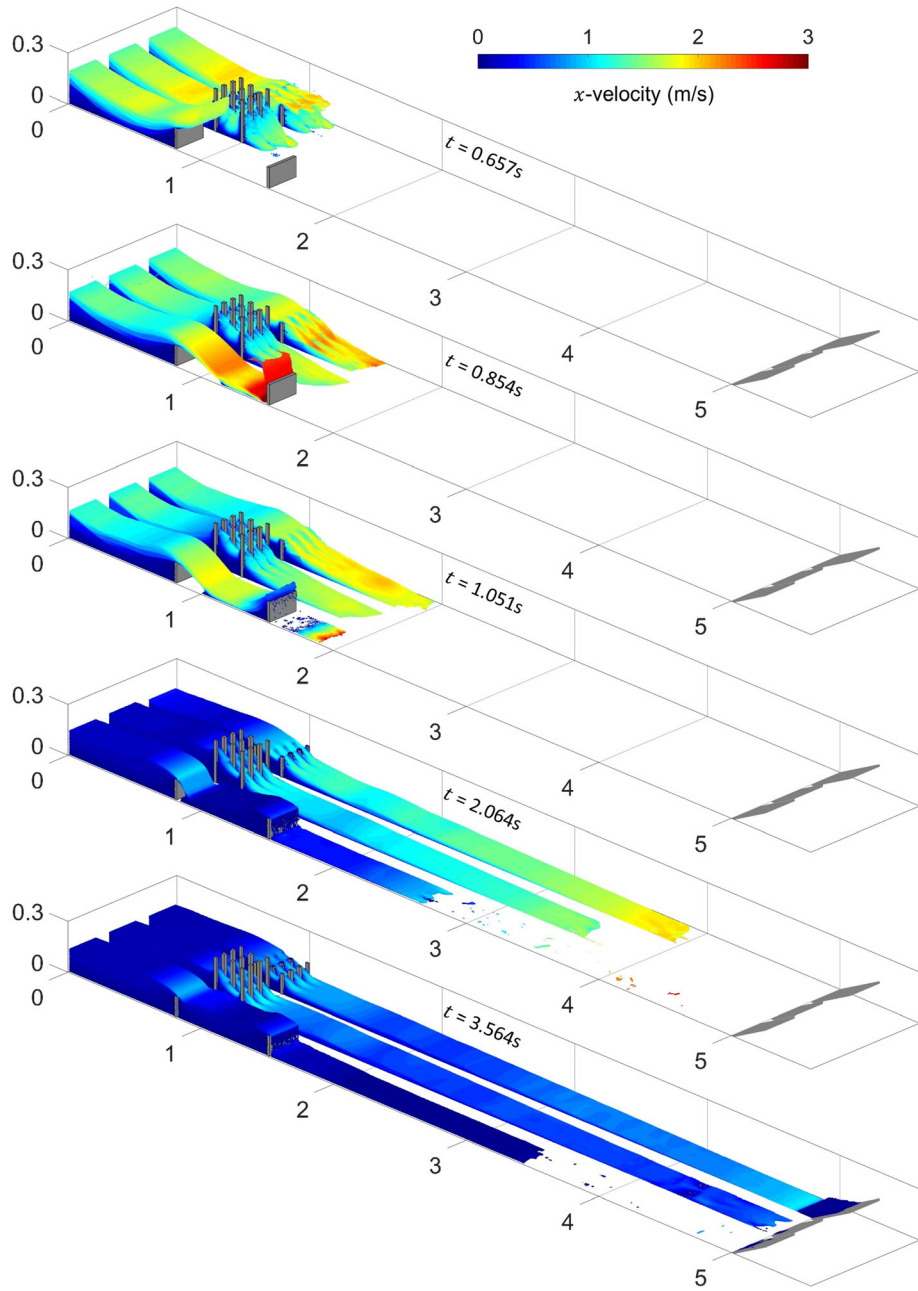


Fig. 15 Flow comparison between baffles 0.12 m tall, 0.25 m tall, and dual barrier system

flow disruption or energy dissipation [10, 51, 79]. Using SPH, we can track the energy in the system without much difficulty. Since the system considered in this paper is entirely mechanical, only the potential and kinetic components of energy need to be considered:

$$E_T(t) = E_K(t) + E_P(t), \quad (36)$$

where $E_T(t)$, $E_K(t)$, and $E_P(t)$, respectively, are the total, kinetic, and potential energy in the system at time t . Strain energy is neglected as its contribution to the total energy is very small (around 1%). In SPH, the total kinetic and

potential energies can be calculated by taking the sum of the kinetic and potential energies of each real SPH particle:

$$E_K(t) = \sum_i \frac{1}{2} m_i v_i^2 \dots E_P(t) = g \sum_i m_i z_i^{'}, \quad (37)$$

where $z_i^{'}$ is the elevation of particle i above a datum (the prime is to differentiate between the z -coordinate in the rotated Cartesian axes). For this analysis, the datum is taken as the bottom of the flume. The cumulative energy dissipated up until time t is simply the difference between

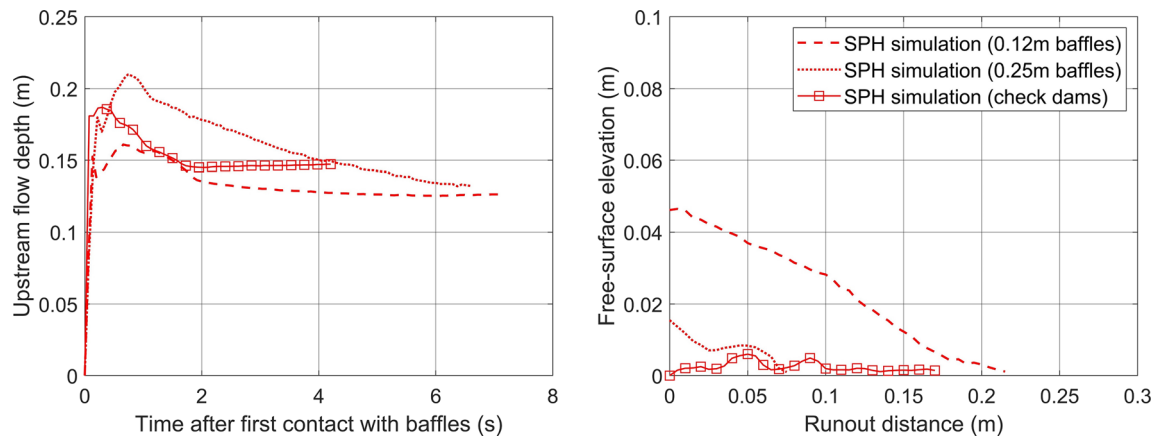


Fig. 16 Upstream flow depth and run-out distances of the dual barrier system

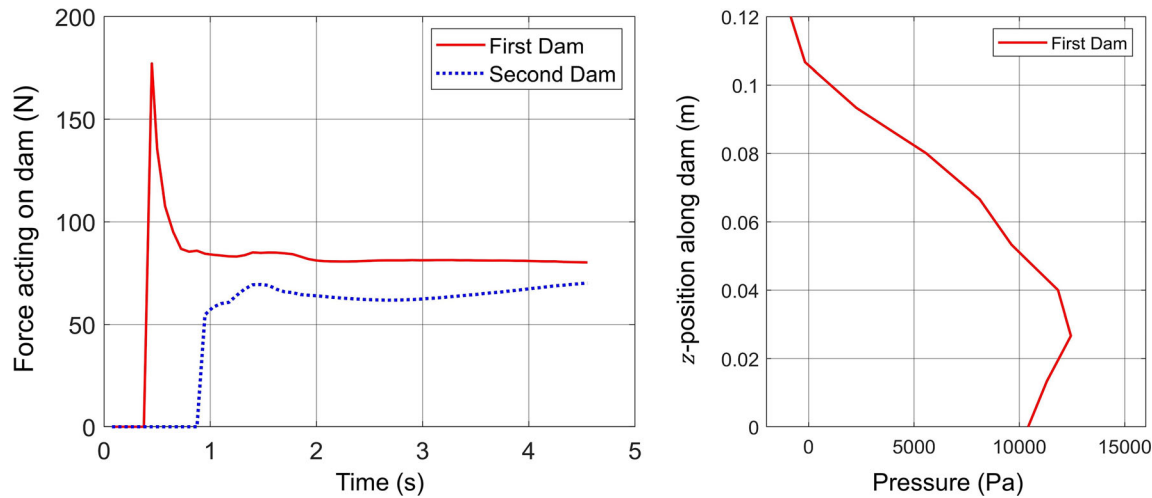


Fig. 17 Force acting on each check dam in dual check-dam system (left) and the pressure profile along the height of the first dam (right)

the initial potential energy, as the granular material is initially static, and the total energy at time t :

$$E_D(t) = E_P(0) - E_T(t), \quad (38)$$

where $E_D(t)$ is the cumulative energy dissipated up until time t .

Figure 18 shows the evolution of the energy in the system for granular flow without baffles and impeded by the 0.12 m and 0.25 m tall baffles and the dual check-dam system. There is significant energy dissipated even without baffles, with almost half the initial energy in the system being dissipated through internal and interfacial friction. Additionally, very little of the initial potential energy is converted to kinetic energy where there are two orders of magnitude difference. At rest, the amount of potential energy is an indication of the volume retained within the flume. When the baffle or dam obstructions are introduced, the total energy dissipated over the entire flow process is less than without any obstructions. But considering the first second of the simulation, for a short duration after the

impact of the flow front with either the baffles or dam, there is an increased energy dissipation when compared to the flows without obstructions. This correlates well with the sharp decrease in kinetic energy, which is indicative of the decelerating effect the baffles or dams have on the flow. Amongst the obstructions considered here, the amount of kinetic energy dissipated is the same, with the kinetic energy being obtained immediately prior to the first impact of the flow front. However, the difference lies in the rate of kinetic energy dissipation. Of the control structures considered, the system using the dual check dams has its kinetic energy brought to zero faster than either baffle cases, and the 0.12 m tall baffles dissipate kinetic energy the slowest. The reverse ordering is obtained for the amount of potential energy remaining in the system once it comes to rest. These findings would suggest that total energy dissipation is not the key to effective debris flow control system. Still, greater kinetic energy dissipation and ensuring high potential energy as the former implies that

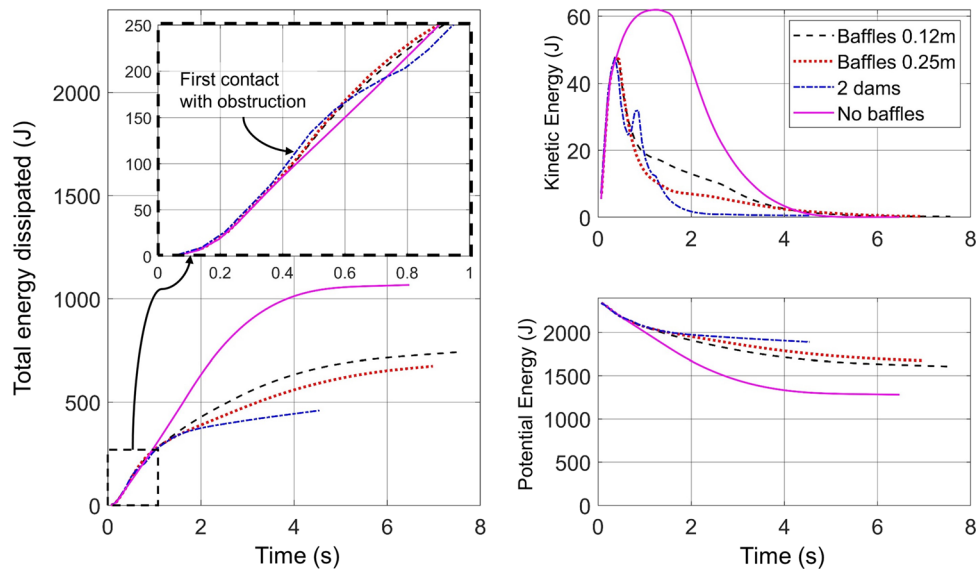


Fig. 18 Total dissipated, kinetic, and potential energy of flow impeded and unimpeded by baffles

the flows are brought to a static state faster, and the latter implies that there is more volume retained upstream.

In addition to energy, we can look at the flow rate of granular material that travels past the obstructions. The flow rate of granular material can be estimated by calculating the volume of material, represented by SPH particles, that travels past some planar surface. Here, we use an x -coordinate to define these planes, which are positioned 1.0 m and 1.5 m downstream from the container. Respectively, they correspond to the end of the baffle region, and the location of the second dam in the dual check-dam system. The outcome of these flow rate calculations is shown in Fig. 19. Without baffles, at the 1.0 m measurement point, the flow swiftly reaches a peak flow of approximately $0.023\text{m}^3/\text{s}$ before gradually descending to $0\text{m}^3/\text{s}$ over around 4 s. The introduction of the 0.12 m drastically reduces the peak flow to approximately

$0.013\text{m}^3/\text{s}$, before decreasing more gradually. There is a slow release of material past the baffle array after that. Increasing the baffle heights to 0.25 m only decreases the peak flow slightly. Looking further downstream at the 1.5 m measurement point shows the difference between the different sized baffles more clearly, with the difference in peak flow rate between the 0.12 m and 0.25 m tall baffles being more pronounced. At the 1.5 m measurement point, the dual check-dam system shows even lower peak flow rates compared to either baffle arrays. These findings suggest that lower peak flow rate is correlated with less run-out.

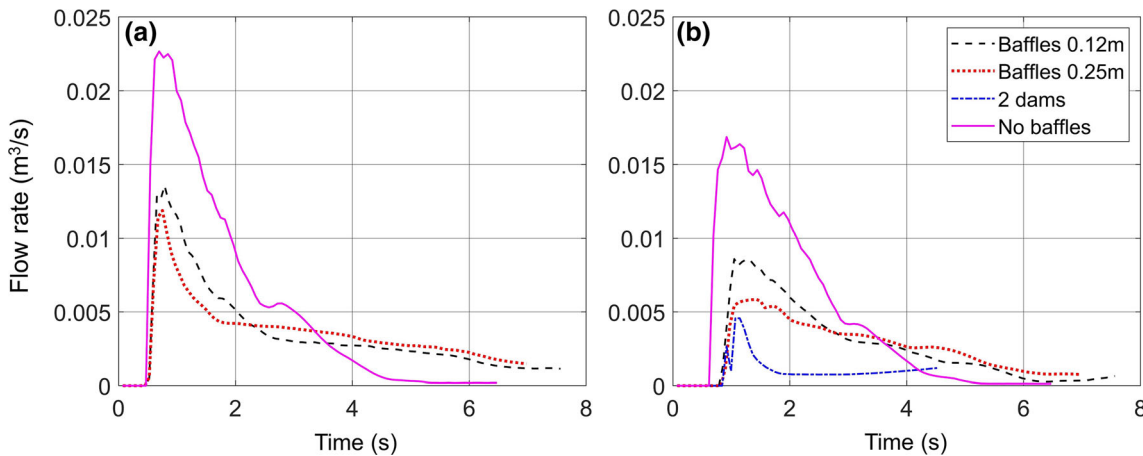


Fig. 19 flow rate measured at (a) 1.0 m and (b) 1.5 m downstream of container

5 Conclusions

In this work, we used the SPH numerical method to investigate the obstruction of granular flows using rigid flow control structures. This was verified by replicating a flume experiment reported in the literature [4, 51, 79]. Here, we investigated the mechanism by which a baffle array or dual check-dam system delays the granular flows and reduces its final run-out. The comparison contributes towards the rationalisation of installing baffles in front of check dams or rigid barriers to reduce design loads, and therefore size of the rigid barriers, as well as contributing to the limited availability of studies on baffles. The control structures are positioned such that the approach flow possesses a maximum Froude number of 3.6. We find that the dual check-dam system is the most effective in preventing material from travelling downstream. Still, height and spacing require careful consideration as material overshooting the first check dam may travel over the second dam without impacting it. Besides, the peak force experienced by the dams is approximately an order of magnitude difference. While we do find that the double check-dam system can be more effective to reduce run-out, because of the greater distance requirements, the topography may not allow for effective placement of check dams. In contrast, baffles can be placed more compactly and still achieve satisfactory outcomes. Also, to improve the effectiveness of the baffles, we find that increasing the height enhances the performance of the baffle array up to a height of approximately 2.7 times the maximum approach flow depth without baffles (for the material properties tested). Increasing the baffle height by this amount prevents some of the granular flow from being able to travel over the baffles unimpeded (i.e. overflow). However, due to the ability of the numerical approach used here to capture both static and dynamic loading, not previously been able to be captured by experimental approaches [79], it can also be highlighted that with an increase in baffle height, the critical design case changes from force due to impact, to force due to volume retention. We note that the conclusions drawn here are for purely channelised conditions and may not apply to flow in more open areas such as basins, mountainsides, or open fields where spreading is allowed, which encourages kinetic energy dissipation.

The conclusions drawn here may not apply to flows with higher Froude numbers, where Froude numbers of 6 are typical for avalanches down mountainsides in Europe [10]. Similarly, the specific recommendations on baffle heights are limited to the material properties tested here, and further investigations are necessary to highlight how the recommendation would change with regard to material properties such as friction angle. Absent from this study

was the use of a constitutive model that possesses the necessary physics to capture the multi-phasic nature of debris flows, as debris flows consist of both granular material and pore air and water, which can alter flows [85]. However, in addition to studying the use of obstructions under non-channelised conditions, this will be left for future work.

Acknowledgements Funding support from the Australian Research Council via Projects DP170103793, DP190102779, and FT200100884, and from NSERC Canada via Project RGPIN-2019-04,155, from the National Natural Science Foundation of China (5,170,091,039), as well as the Research Grants Council of Hong Kong (16,212,618; 16,209,717; 16,210,219; T22-603/15 N; AoE/E-603/18), is gratefully acknowledged. This research was undertaken with the assistance of resources and services from the National Computational Infrastructure (NCI), which is supported by the Australian Government.

References

1. Iverson RM, Schilling SP, Vallance JW (1998) Objective delineation of lahar-inundation hazard zones. *GSA Bulletin* 110(8):972–984
2. Jakob M, Weatherly H (2003) A hydroclimatic threshold for landslide initiation on the North Shore Mountains of Vancouver British Columbia. *Geomorphology* 54(3):137–156
3. Rosser B et al (2017) New Zealand's National Landslide Database. *Landslides* 14(6):1949–1959
4. Choi C et al (2015) Computational investigation of baffle configuration on impedance of channelized debris flow. *Can Geotech J* 52(2):182–197
5. Mizuyama T (2008) Structural countermeasures for debris flow disasters. *Int J Erosion Control Eng* 1(2):38–43
6. Wendeler C et al (2008) Hazard prevention using flexible multi-level debris flow barriers. *Proc of Int Symp Interpraevent* 1:547–554
7. Choi KY, Cheung RWM (2013) Landslide disaster prevention and mitigation through works in Hong Kong. *J Rock Mech Geotech Eng* 5(5):354–365
8. Cosenza E et al (2006) Concrete structures for mitigation of debris-flow hazard in the Montoro Inferiore Area, Southern Italy
9. Ng CWW et al (2018) Dry granular flow interaction with dual-barrier systems. *Géotechnique* 68(5):386–399
10. Hákonardóttir KM et al (2003) A laboratory study of the retarding effects of braking mounds on snow avalanches. *J Glaciol* 49(165):191–200
11. Jóhannesson T et al (2008) The design of avalanche protection dams. Recent practical and theoretical developments
12. Lau C, Chan E, Kwan J (2012) Natural terrain hazard mitigation measures
13. Kwan J (2012) Supplementary technical guidance on design of rigid debris-resisting barriers. Geotechnical Engineering Office, HKSAR. GEO Report, p 270
14. Kwan J, Koo R, Lam C (2018) Review on the design of rigid debris-resisting barriers
15. Major JJ (1997) Depositional processes in large-scale debris-flow experiments. *J Geol* 105(3):345–366
16. Naaim M et al (2010) Return period calculation and passive structure design at the Taconnaz avalanche path France. *Ann Glaciol* 51(54):89–97

17. Sulsky D, Chen Z, Schreyer HL (1994) A particle method for history-dependent materials. *Comput Methods Appl Mech Eng* 118(1–2):179–196
18. Zhang X et al (2013) Particle finite element analysis of large deformation and granular flow problems. *Comput Geotech* 54:133–142
19. Soga K et al (2016) Trends in large-deformation analysis of landslide mass movements with particular emphasis on the material point method. *Géotechnique* 66(3):248–273
20. Lucy LB (1977) A numerical approach to the testing of the fission hypothesis. *Astronom J* 82:1013–1024
21. Gingold RA, Monaghan JJ (1977) Smoothed particle hydrodynamics: theory and application to non-spherical stars. *Mon Not R Astron Soc* 181(3):375–389
22. Cundall PA, Strack OD (1979) A discrete numerical model for granular assemblies. *Géotechnique* 29(1):47–65
23. Monaghan JJ (1994) Simulating free surface flows with SPH. *J Comput Phys* 110(2):399–406
24. Libersky LD, Petschek AG (1991) Smooth particle hydrodynamics with strength of materials. Springer, Berlin
25. Bui HH et al (2008) Lagrangian meshfree particles method (SPH) for large deformation and failure flows of geomaterial using elastic–plastic soil constitutive model. *Int J Numer Anal Meth Geomech* 32(12):1537–1570
26. Pastor M et al (2009) A depth-integrated, coupled SPH model for flow-like landslides and related phenomena. *Int J Numer Anal Meth Geomech* 33(2):143–172
27. Bui HH et al (2011) Slope stability analysis and discontinuous slope failure simulation by elasto-plastic smoothed particle hydrodynamics (SPH). *Géotechnique* 61(7):565–574
28. Nonoyama H et al (2015) Slope stability analysis using smoothed particle hydrodynamics (SPH) method. *Soils Found* 55(2):458–470
29. Bui HH, Nguyen GD (2017) A coupled fluid-solid SPH approach to modelling flow through deformable porous media. *Int J Solids Struct* 125:244–264
30. Bui HH, Sako K, Fukagawa R (2007) Numerical simulation of soil–water interaction using smoothed particle hydrodynamics (SPH) method. *J Terramech* 44(5):339–346
31. Tran HT et al (2019) Modelling 3D desiccation cracking in clayey soils using a size-dependent SPH computational approach. *Comput Geotech* 116:103209
32. Wang Y et al (2020) Simulation of mixed-mode fracture using SPH particles with an embedded fracture process zone. *Int J Numer Anal Methods Geomech*
33. Wang Y et al (2019) A new SPH-based continuum framework with an embedded fracture process zone for modelling rock fracture. *Int J Solids Struct* 159:40–57
34. Chen W, Qiu T (2012) Numerical simulations for large deformation of granular materials using smoothed particle hydrodynamics method. *Int J Geomech* 12(2):127–135
35. Favero A, Borja R (2018) Continuum hydrodynamics of dry granular flows employing multiplicative elastoplasticity. *Acta Geotech*
36. Ghaïtanellis A et al (2018) A SPH elastic-viscoplastic model for granular flows and bed-load transport. *Adv Water Resour* 111:156–173
37. He X et al (2018) Study of the interaction between dry granular flows and rigid barriers with an SPH model. *Int J Numer Anal Meth Geomech* 42(11):1217–1234
38. Longo A et al (2019) A depth average SPH model including μ (I) rheology and crushing for rock avalanches. *Int J Numer Anal Meth Geomech* 43(5):833–857
39. Neto AHF, Borja RI (2018) Continuum hydrodynamics of dry granular flows employing multiplicative elastoplasticity. *Acta Geotech* 13(5):1027–1040
40. Nguyen CT et al (2017) A new SPH-based approach to simulation of granular flows using viscous damping and stress regularisation. *Landslides* 14(1):69–81
41. Manzanal D et al (2016) Application of a new rheological model to rock avalanches: an SPH approach. *Rock Mech Rock Eng* 49(6):2353–2372
42. Nguyen NH, Bui HH, Nguyen GD (2020) Effects of material properties on the mobility of granular flow. *Granular Matter* 22:59
43. Bui H, Nguyen GD (2020) Numerical predictions of post-flow behaviour of granular materials using an improved SPH model. In: CIGOS 2019, innovation for sustainable infrastructure. Springer, Berlin, p 895–900
44. Bui HH et al (2014) A novel computational approach for large deformation and post-failure analyses of segmental retaining wall systems. *Int J Numer Anal Meth Geomech* 38(13):1321–1340
45. Bui HH et al (2008) SPH-based numerical simulations for large deformation of geomaterial considering soil–structure interaction. In: The 12th international conference of international association for computer methods and advances in geomechanics (IACMAG). 2008.
46. Faug T (2015) Macroscopic force experienced by extended objects in granular flows over a very broad Froude-number range. *Europ Phys J E* 38(5):1–10
47. Peng C et al (2019) LOQUAT: an open-source GPU-accelerated SPH solver for geotechnical modeling. *Acta Geotech* 14(5):1269–1287
48. Yang E et al (2020) A scalable parallel computing SPH framework for predictions of geophysical granular flows. *Comput Geotech* 121:103474
49. Valdez-Balderas D et al (2013) Towards accelerating smoothed particle hydrodynamics simulations for free-surface flows on multi-GPU clusters. *J Parallel Distrib Comput* 73(11):1483–1493
50. Oger G et al (2016) On distributed memory MPI-based parallelization of SPH codes in massive HPC context. *Comput Phys Commun* 200:1–14
51. Ng CWW et al (2015) Physical modeling of baffles influence on landslide debris mobility. *Landslides* 12(1):1–18
52. Naaim M, Faug T, Naaim-Bouvet F (2003) Dry granular flow modelling including erosion and deposition. *Surv Geophys* 24(5–6):569–585
53. Kattel P et al (2018) Interaction of two-phase debris flow with obstacles. *Eng Geol* 242:197–217
54. Dehnen W, Aly H (2012) Improving convergence in smoothed particle hydrodynamics simulations without pairing instability. *Mon Not R Astron Soc* 425(2):1068–1082
55. Antuono M et al (2010) Free-surface flows solved by means of SPH schemes with numerical diffusive terms. *Comput Phys Commun* 181(3):532–549
56. Oger G et al (2007) An improved SPH method: Towards higher order convergence. *J Comput Phys* 225(2):1472–1492
57. Blanc T, Pastor M (2013) A stabilized Smoothed Particle Hydrodynamics, Taylor-Galerkin algorithm for soil dynamics problems. *Int J Numer Anal Meth Geomech* 37(1):1–30
58. Moriguchi S et al (2009) Estimating the impact force generated by granular flow on a rigid obstruction. *Acta Geotech* 4(1):57–71
59. Moriguchi S et al (2005) Numerical simulation of flow failure of geomaterials based on fluid dynamics. *Soils Found* 45(2):155–165
60. Uzuoka R (2000) Analytical study on the mechanical behavior and prediction of soil liquefaction and flow. Ph. D. Dissertation, Gifu University
61. Lagrée P-Y, Staron L, Popinet S (2011) The granular column collapse as a continuum: validity of a two-dimensional Navier–Stokes model with a μ (I)-rheology. *J Fluid Mech* 686:378–408

62. Papanastasiou TC (1987) Flows of materials with yield. *J Rheol* 31(5):385–404
63. Adami S, Hu XY, Adams NA (2012) A generalized wall boundary condition for smoothed particle hydrodynamics. *J Comput Phys* 231(21):7057–7075
64. Morris JP, Fox PJ, Zhu Y (1997) Modeling low reynolds number incompressible flows using SPH. *J Comput Phys* 136(1):214–226
65. Marrone S et al (2011) Computer methods in applied mechanics and engineering. *Comput Method Appl Mech Eng* 200:1526–1542
66. Nomeritae N et al (2016) Explicit incompressible SPH algorithm for free-surface flow modelling: a comparison with weakly compressible schemes. *Adv Water Resour* 97:156–167
67. Liu M, Shao J, Chang J (2012) On the treatment of solid boundary in smoothed particle hydrodynamics. *Sci China Technol Sci* 55(1):244–254
68. Liu GR, Liu MB (2003) Smoothed Particle Hydrodynamics: A Meshfree Particle Method
69. Cui X, Gray J (2013) Gravity-driven granular free-surface flow around a circular cylinder. *J Fluid Mech* 720:314–337
70. Monaghan JJ (1992) Smoothed particle hydrodynamics. *Ann Rev Astron Astrophys* 30(1):543–574
71. Monaghan JJ (2000) SPH without a tensile instability. *J Comput Phys* 159(2):290–311
72. Lind SJ et al (2012) Incompressible smoothed particle hydrodynamics for free-surface flows: a generalised diffusion-based algorithm for stability and validations for impulsive flows and propagating waves. *J Comput Phys* 231(4):1499–1523
73. Sun PN et al (2017) The δ -plus-SPH model: Simple procedures for a further improvement of the SPH scheme. *Comput Methods Appl Mech Eng* 315:25–49
74. Khayyer A, Gotoh H, Shimizu Y (2017) Comparative study on accuracy and conservation properties of two particle regularization schemes and proposal of an optimized particle shifting scheme in ISPH context. *J Comput Phys* 332:236–256
75. Xu R, Stansby P, Laurence D (2009) Accuracy and stability in incompressible SPH (ISPH) based on the projection method and a new approach. *J Comput Phys* 228(18):6703–6725
76. Colagrossi A et al (2012) Particle packing algorithm for SPH schemes. *Comput Phys Commun* 183(8):1641–1653
77. Terzaghi K (1943) Arching in ideal soils. *Theor Soil Mech*, pp 66–76
78. Staron L, Lagrée P-Y, Popinet S (2014) Continuum simulation of the discharge of the granular silo: a validation test for the $\mu(I)$ visco-Plastic flow law. *Europhys J E Soft Matter* 37:9961
79. Choi CE et al (2014) Flume investigation of landslide debris-resisting baffles. *Can Geotech J* 51(5):540–553
80. Marrone S et al (2010) Fast free-surface detection and level-set function definition in SPH solvers. *J Comput Phys* 229(10):3652–3663
81. Chambon G et al (2011) Numerical simulations of granular free-surface flows using smoothed particle hydrodynamics. *J Non-newton Fluid Mech* 166(12–13):698–712
82. Kwan J (2012) Supplementary technical guidance on design of rigid debris-resisting barriers
83. Koo R et al (2017) Velocity attenuation of debris flows and a new momentum-based load model for rigid barriers. *Landslides* 14(2):617–629
84. Van Dine D (1996) Debris flow control structures for forest engineering. Research Branch BC Min For, Victoria, BC, Working Paper, vol 8
85. Iverson RM (1997) The physics of debris flows. *Rev Geophys* 35(3):245–296

Publisher's Note Springer Nature remains neutral with regard to jurisdictional claims in published maps and institutional affiliations.